Title
Barrier-free contact to MoS2 transistor and the transport properties of its localized states

Author
Wu, Hao

Publication Date
2017

Peer reviewed|Thesis/dissertation

UNIVERSITY OF CALIFORNIA

Los Angeles

Barrier-free contact to MoS_2 transistor and the transport properties of its localized states

A dissertation submitted in partial satisfaction of the requirements for the degree Doctor of Philosophy in Materials Science and Engineering

by

Hao Wu

2018

ABSTRACT OF THE DISSERTATION

Barrier-free contact to MoS_2 transistor and the transport properties of its localized states

by

Hao Wu

Doctor of Philosophy in Materials Science and Engineering

University of California, Los Angeles, 2018

Professor Yu Huang, Chair

The two-dimensional layered materials such as molybdenum disulfide (MoS_2) have attracted tremendous interest as a new class of electronic materials. However, there are considerable challenges in replacing silicon with two-dimensional materials to build large-scale integrated circuits in the semiconductor industry. The commercialization of two-dimensional layered materials requires further enhancement of the electronic device performance. Therefore, the reliable device contact and carrier transport are significantly important. Here I would present a new protocol to make barrier-free contact to MoS_2 transistor and an algorithm to profile the localized states based on the transport properties of MoS_2 transistors.

The dissertation of Hao Wu is approved.

Dwight Streit

Xiangfeng Duan

Yu Huang, Committee Chair

University of California, Los Angeles

2018

Table of contents

Acknowledgments

Foremost, I would like to express my gratitude to my advisors Dr. Yu Huang and Dr. Xiangfeng Duan for their guidance. It is a pleasure to be a student working with them. They are the most valuable resources I have at UCLA. Their broad knowledge and vision help me to grow from an undergraduate student who knows almost nothing about research to a fully-fledged researcher with my own insight into the IT industry. I really appreciate the freedom they give me. It allows me to explore other technical fields in the IT industry. Being their student not only benefit me for my career but also for my whole life. I am also thankful for the other members of my degree committee: Dr. Dwight Streit and Dr. Qibing Pei. They gave me a lot of support and constructive advices all through my study at UCLA. My acknowledgement also goes to Dr. Vidvuds Ozolins, who was my co-advisor in my first few years at UCLA.

Besides, I am grateful for Dr. Will Conley, Ms. Tessa Villasenor, and Dr. Sharmilla Venugopal. In 2017, I worked as a programming lab teaching assistant with them. The TAship saved me out of funding crisis and landed me a job as software engineer after graduation. I will always remember their help.

My sincere thanks are extended to my colleagues, friends, and relatives: Dr. Dehui Li, Dr. Hung-Chieh Cheng, Dr. Enbo Zhu, Dr. Yuan Liu, Mr. Sen Yang, Mr. Jian Guo, Mr. Zeyu Deng, Ms. Yun-Chiao Huang, Dr. Rui Cheng, Dr. Chin-Yi Chiu, Dr. Qiyuan He,

Dr. Mengning Ding, Dr. Yongjia Li, Mr. Yiliu Wang, Dr. Fanli Meng, Mr. Tyler Scholes, Dr. Yang Wang, Dr. Gongming Wang, Dr. Anxiang Yin, Dr. Jonathan Shaw, Dr. Fei Zhou, Ms. Yujia Peng, Dr. Héctor Alcalá, Dr. Xiao Yan, Dr. Zheng Xing, Mr. Hoc Ngo, Ms. Huiying Shiu, Mr. Sung Joon Lee, Dr. Chen Wang, Dr. Xiaoxing Lu, Mr. Kirti Dhwaj, Ms. Laura Bluth, Mr. Weisheng Wang, Mr. Xiating Ouyang, Ms. Bing Xia, Mr. Shu Wang, Mr. Qing Xia, Mr. Xiaofeng Du, Dr. Yifan Xia. They are always there to support me. To Dr. Dehui Li, Dr. Hung-Chieh Cheng, Dr. Enbo Zhu and Dr. Yuan Liu, your help and encouragement mean a lot to me! Thank you!

Last but not the least, I would like to give my special thanks to my parents, Mr. Zhongquan Wu and Ms. Hui Wang. It is their continuous support and unconditional love that makes me become the person that I am today. They raised me up, encouraging me in all of my pursuits and inspiring me to follow my dreams. I believe in the love and eternity of my family. Life is a long and sometimes bumpy road but the love of family will always get me through any difficulties.

Hao Wu

University of California, Los Angeles

December 2017

Biography

Hao Wu received his B.S. degree of physics from the science and engineering honor program at Nankai University, China in 2011. He then joined the department of Materials Science and Engineering at University of California, Los Angeles to pursue a Ph.D. degree. He conducted research under the guidance of Dr. Yu Huang on the fabrications, simulations and applications of novel semiconductor device. He co-authored sixteen papers in peer-reviewed journals during his study at UCLA. His research interests include scientific programming, semiconductor physics, and wearable device applications.

Chapter 1 General Introduction

Moore's law slowing down

Moore's law is the observation that the transistor density on integrated circuit chips would be doubled and the characterization size of transistor would be halved every eighteen months[1,2]. In the last few decades, the Moore's law has been driving the scaling down of transistor[3,4]. However, with the shrinking size of transistors, the short channel effects are becoming more and more severe[5]. Specifically, the gate capacitance control over the channel current would become much weaker[6-8]. Therefore, the scaling down trend is slowing down after year 2010[4]. In order to extend the continuing progress of Moore's law, multiple novel device designs have been proposed[9-12].

In the current semiconductor manufacturing industry, FinFET structure is utilized after the 22 nm nodes to solve the problem of weak gate control[6,13,14]. For the conventional planar MOSFET structure, the transistor is composed of a planar polysilicon gate electrode and planar silicon substrate. In contrast, the gate electrode of FinFET wraps around the channel region providing a better electrostatic control over the channel current. Although FinFET exhibits great short-channel behavior, its structure poses new technical challenges such as higher aspect ratios of the Fin structure. As illustrated in the data published by Intel[15], the aspect ratio of Fin structure is increasing from 1 to 6 as the characterization length of device is shrinking

from 22 nm to 10 nm, which inevitability introduces difficulties into the fabrication processes. To circumvent such fabrication difficulties, the thickness of transistor channel can be reduced to nanometer scale in order to decrease the leakage region in the channel[16,17]. This method has been theoretically proved to be an effective approach to improve the performance. However in practice, the electron would be subject to extremely large surface scattering because of the surface roughness[18]. Therefore, in the IRDS (International Roadmap for Device and System) of 2017[19], transition to the new device architecture and exploring new high-mobility channel material (such as Geminium and other III-V materials) are listed as the focuses of future research. Meanwhile, the two-dimensional semiconductor materials are also considered as an excellent candidate for the next-generation device in the research community[7].

The rise of two-dimensional materials

The two-dimensional materials generally represent a class of novel layered materials whose each layer is weakly coupled to each other via Van der Waals forces[20-22]. The first two-dimensional material discovered is grapheme, which is a single layer of carbon atom[20]. The two-dimensional crystal structure of graphene comes from the interactions of carbon-carbon σ bonds and sp2 hybridization[23]. The weak interaction between the adjacent graphene layers allows the easy mechanical exfoliation and leads to its discovery[24]. Ever since its discovery, graphene has become the star of the

fundamental physics studies and its tremendous physical and chemical properties have triggered numerous electronic device researches as well[20]. Due to the unique symmetry of graphene unit-cell geometry, it shows a semimetal (zero band-gap) property as its conduction band and valence band degenerate at the K-points of Brillouin zone[25]. Moreover, the band structure of graphene has a special linear dispersion in the vicinity of K-points, thus leading to extremely high carrier mobility and outstanding heat conductivity. Apart from these two characteristics, its good flexibility and transparency also make graphene an exceptionally good material for electronic device[26,27]. But unfortunately, the logic electronic device requires a sizeable band-gap to achieve certain on-off ratio and energy consumptions.

Although there have been multiple attempts to open up the graphene band-gap (such as graphene nanoribbon[28], AB-stack bilayer graphene[29], hydrogenated graphene[30]), the as-produced graphene device unfortunately suffers from the higher crystal-structure defect densities and results in the low carrier mobility. Therefore, in recent years, the research focus has been shifted to the studies of two-dimensional semiconductor materials. One of the most studied classes of two-dimensional semiconductor materials is transition metal dichalcogenide (TMD)[21,22,27]. The intrinsic bandgap of some TMD materials address the zero-bandgap problem of graphene. In addition, as the research evolves, more intriguing properties of TMD are demonstrated, such as metal-insulator transition[31], superconductivity[32] and Shubnikov–de Haas oscillations[33]. Besides, the atomically thin geometry of 2D

semiconductors may promise lower power dissipation electronic devices for integrated circuits, and the direct bandgap monolayer materials have generated considerable interests for diverse electric and optoelectronic applications[34-36].

However, the attained field-effect mobilities in the device fabricated with two-dimensional semiconductor materials are still considerably lower than the theoretically predicted value[37]. This has largely stalled the further application and commercialization of two-dimensional semiconductor materials in the semiconductor industry. Recent studies have attribute the low motilities to the contact barrier and intrinsic scattering within the materials[38,39].

Therefore, in my dissertation, I would like to use MoS_2 as an example of two-dimensional semiconductor materials, to demonstrate the approach to barrier-free contact of the field-effect transistors. Then I would utilize the barrier-free MoS_2 transistor as the platform to study the carrier transport properties and opens up the possibility to further enhance the MoS_2 electrical properties.

In the chapter 2, I would present a new strategy by using graphene as the back electrodes to achieve Ohmic contact to MoS_2 in the chapter 2. With a finite density of states, the Fermi level of graphene can be readily tuned by a gate potential to enable a nearly perfect band alignment with MoS_2. I would demonstrate for the first time a transparent contact to MoS_2 with zero contact barrier and linear output behavior at

cryogenic temperatures (down to 1.9 K) for both monolayer and multilayer MoS_2. Benefiting from the barrier-free transparent contacts, I show that a metal−insulator transition can be observed in a two-terminal MoS_2 device, a phenomenon that could be easily masked by Schottky barriers found in conventional metal-contacted MoS_2 devices. With further passivation by boron nitride (BN) encapsulation, I would demonstrate a record-high extrinsic (two-terminal) field effect mobility up to 1300 $cm^2/(V\ s)$ in MoS_2 at low temperature.

In the Chapter 3, I would demonstrate the simulations of the graphene MoS_2 contact. In the framework of tight-binding model of graphene and Poisson equation of the electrons at the interface, the barrier was systematically studied with several tuning parameters. With the varying graphene stacks thickness and the varying carrier concentration of MoS_2, the tunable work function range also changes. It is discovered that with the graphene thickness reduced to the monolayer and carrier concentration of MoS_2 above a threshold value, the barrier between graphene and MoS_2 can be tuned to 0 meV.

In the Chapter 4, I will show that the field-modulated conductivity change can be used to probe the electronic structure of the localized states in monolayer MoS_2. This would provide us a fundamental understanding of the charge transport mechanism in two-dimensional semiconductors (e.g., MoS_2), which is crucial for fully exploring their potential in electronic and optoelectronic devices. A series of regularly

distributed plateaus were observed in the gate-dependent transfer curves. Our theoretical calculations based on the variable range hopping theory indicate that such plateaus can be attributed to the discrete localized states in the vicinity of mobility edge. Our approach provides establishes an effective approach for directly the localized states in the MoS_2 conduction channel with an ultrahigh resolution up to 1 meV.

In the Chapter 5, I would dive deep into the simulations of the localized state transport. Based on the variable range hopping model and the gate capacitance model, the localized states' electronic structure can be profiled. Finally, the vectorization of transport equations will also be demonstrated in order to leverage the parallel computer architecture, thus speeding up the computation.

References

1 Moore, G. E. Cramming more components onto integrated circuits (Reprinted from Electronics, pg 114-117, April 19, 1965). *IEEE Solid-State Circuits Society Newsletter* **86**, 82-85 (1998).

2 Schaller, R. R. Moore's Law: Past, present, and future. *IEEE Spectr.* **34**, 52-59 (1997).

3 Mack, C. A. Fifty Years of Moore's Law. *IEEE Trans. Semicond. Manuf.* **24**, 202-207, (2011).

4 Waldrop, M. M. The chips are down for Moore's law. *Nature* **530**, 144-147 (2016).

5 Kim, N. S. *et al.* Leakage current: Moore's law meets static power. *Computer* **36**, 68-75 (2003).

6 Chang, L. L. *et al.* Moore's law lives on - Ultra-thin body SOI and FinFET CMOS transistors look to continue Moore's law for many years to come. *IEEE Circuits Device* **19**, 35-42 (2003).

7 Vogel, E. M. Technology and metrology of new electronic materials and devices. *Nat. Nanotechnol.* **2**, 25-32 (2007).

8 Muller, D. A. A sound barrier for silicon? *Nat. Mater.* **4**, 645-647 (2005).

9 Chen, X. G. *et al.* Interfacial Charge Engineering in Ferroelectric-Controlled Mott Transistors. *Adv. Mater.* **29** 1701385 (2017).

10 Mikolajick, T., Heinzig, A., Trommer, J., Baldauf, T. & Weber, W. M. The RFET-a reconfigurable nanowire transistor and its application to novel electronic

circuits and systems. *Semicond. Sci. Technol.* **32** 043001 (2017).

11 Hutchby, J. A., Bourianoff, G. L., Zhirnov, V. V. & Brewer, J. E. Emerging research memory and logic technologies - A critical review of the technologies based on a new relevance/evaluation criteria. *IEEE Circuits Device* **21**, 47-51 (2005).

12 Reed, M. A. & Tour, J. M. Computing with molecules. *Sci. Am.* **282**, 86-93 (2000).

13 Hisamoto, D. *et al.* FinFET - A self-aligned double-gate MOSFET scalable to 20 nm. *IEEE Trans. Electron Devices* **47**, 2320-2325 (2000).

14 Xiong, S. Y. & Bokor, J. Sensitivity of double-gate and FinFET devices to process variations. *IEEE Trans. Electron Devices* **50**, 2255-2261 (2003).

15 Mistry, K. Leading at the edge. (2017). at https://newsroom.intel.com/press-kits/leading-edge-intel-technology-manufacturing/

16 Choi, Y.-K. *et al.* Ultra-thin body SOI MOSFET for deep-sub-tenth micron era. *Tech. Digest.- Int. Electron Devices Meet.* 919-921, doi:10.1109/IEDM.1999.824298 (1999).

17 Choi, Y. K., Ha, D., King, T. J. & Bokor, J. Investigation of gate-induced drain leakage (GIDL) current in thin body devices: Single-gate ultra-thin body, symmetrical double-gate, and asymmetrical double-gate MOSFETs. *Jpn. J. Appl. Phys. 1* **42**, 2073-2076 (2003).

18 Jin, S. H., Fischetti, M. V. & Tang, T. W. Modeling of surface-roughness scattering in ultrathin-body SOI MOSFETs. *IEEE Trans. Electron Devices* **54**, 2191-2203 (2007).

19 IEEE. Beyond CMOS White Paper. *International Roadmap for Devices and Systems, 2016 Edition* (2016)

20 Geim, A. K. & Novoselov, K. S. The rise of graphene. *Nat. Mater.* **6**, 183-191 (2007).

21 Radisavljevic, B., Radenovic, A., Brivio, J., Giacometti, V. & Kis, A. Single-layer MoS2 transistors. *Nat. Nanotechnol.* **6**, 147-150 (2011).

22 Zhao, W. J. *et al.* Evolution of Electronic Structure in Atomically Thin Sheets of WS2 and WSe2. *Acs Nano* **7**, 791-797 (2013).

23 Yao, Y. G., Ye, F., Qi, X. L., Zhang, S. C. & Fang, Z. Spin-orbit gap of graphene: First-principles calculations. *Phys. Rev. B* **75**, 041401(2007).

24 Novoselov, K. S. *et al.* Electric field effect in atomically thin carbon films. *Science* **306**, 666-669 (2004).

25 Partoens, B. & Peeters, F. M. From graphene to graphite: Electronic structure around the K point. *Phys. Rev. B* **74**, 075404(2006).

26 Kim, K. S. *et al.* Large-scale pattern growth of graphene films for stretchable transparent electrodes. *Nature* **457**, 706-710 (2009).

27 Georgiou, T. *et al.* Vertical field-effect transistor based on graphene-WS2 heterostructures for flexible and transparent electronics. *Nat. Nanotechnol.* **8**, 100-103 (2013).

28 Li, X. L., Wang, X. R., Zhang, L., Lee, S. W. & Dai, H. J. Chemically derived, ultrasmooth graphene nanoribbon semiconductors. *Science* **319**, 1229-1232 (2008).

29 Zhang, Y. B. *et al.* Direct observation of a widely tunable bandgap in bilayer

graphene. *Nature* **459**, 820-823 (2009).

30 Elias, D. C. *et al.* Control of Graphene's Properties by Reversible Hydrogenation: Evidence for Graphane. *Science* **323**, 610-613 (2009).

31 Radisavljevic, B. & Kis, A. Mobility engineering and a metal-insulator transition in monolayer MoS2. *Nat. Mater.* **12**, 815-820 (2013).

32 Ye, J. T. *et al.* Superconducting Dome in a Gate-Tuned Band Insulator. *Science* **338**, 1193-1196 (2012).

33 Cui, X. *et al.* Multi-terminal transport measurements of MoS2 using a van der Waals heterostructure device platform. *Nat. Nanotechnol.* **10**, 534-540 (2015).

34 Cheng, R. *et al.* Few-layer molybdenum disulfide transistors and circuits for high-speed flexible electronics. *Nat. Commun.* **5** (2014).

35 Tian, H. *et al.* Optoelectronic devices based on two-dimensional transition metal dichalcogenides. *Nano. Res.* **9**, 1543-1560 (2016).

36 Wan, X. *et al.* Controlled Electrochemical Deposition of Large-Area MoS2 on Graphene for High-Responsivity Photodetectors. *Adv. Funct. Mater.* **27**, 1603998 (2017).

37 Yu, Z. H. *et al.* Towards intrinsic charge transport in monolayer molybdenum disulfide by defect and interface engineering. *Nat Commun* **5** (2014).

38 Liu, Y. *et al.* Toward Barrier Free Contact to Molybdenum Disulfide Using Graphene Electrodes. *Nano Lett.* **15**, 3030-3034 (2015).

39 Kaasbjerg, K., Thygesen, K. S. & Jacobsen, K. W. Phonon-limited mobility in n-type single-layer MoS2 from first principles. *Phys. Rev. B* **85**, 115317(2012).

Chapter 2 Contact engineering of graphene electrode to MoS_2 field effect transistor

Introduction

MoS_2, as a two-dimensional material has attracted a lot research interest and is considered as the material to replace silicon for next-generation electronics[1-11]. However, its promise is hindered due to the difficulties in fabricating perfect contact to the field-effect transistor. Considerable efforts have been devoted to decreasing the contact resistance, such as using low work function metal electrodes, high temperature annealing, and phase engineering[12-20]. However, such approaches are still not possible to achieve linear Ohmic contact. Particularly, the Schottky barrier would dominate the transport behaviour at low temperature. Fermi level pinning is generally considered as the primary reason of the nonlinear behaviour of contact for conventional metal-contacted device[12]. The large contact resistance not only remains a major bottleneck to optimize the device performance, but also prevents the investigation of MoS_2 intrinsic properties, such as the observation of quantum transport behaviour at cryogenic temperature.

Herein I present a protocol to use single-layer graphene as an adaptable contact to achieving Ohmic contact to the atom-thin semiconductors. As the density of states are finite in the vicinity of Dirac cone, graphene's Fermi level can be modified by the nearby material without difficulties, thus resulting in an adaptable work function.

Specifically, the nearby MoS_2 will dope the graphene, therefore increasing the Fermi level. The lined-up Fermi levels of graphene and MoS_2 ensure a nearly perfect work function match with MoS_2. Besides, systematic investigations of grpahene-MoS_2 contact are also conducted using variable thickness graphene. The results show that the barrier height increases with the increasing number of graphene layers, which can be attributed to the fact that increased density of state in thicker graphene makes the Fermi level more unadjustable. Importantly, I demonstrated that a monolayer graphene contacts are essential to achieve transparent contact to MoS_2 without little contact barrier. For the first time, the linear output behaviours are achieved at cryogenic temperatures down to 1.9 K. With the barrier-free carrier transparent contacts, the MoS_2 field-effect transistors show a metal-insulator-transition (MIT). This phenomenon could only be observed in in four-terminal devices while in our experiment it was observed in a two-terminal device. The reason is that the transition was easily masked by Schottky barrier in conventional metal-contacted MoS_2 system. Furthermore, with the minimized contact barrier and reduced contact resistance, the graphene-contacted devices display the record high extrinsic (two-terminal) field effect mobility (1300 cm^2/ V s). I believe that the strategy of using graphene as the adaptable barrier free contact could generally address the contact engineering problem of 2D material transistor and shed light on other conventional transistors in general.

Device fabrication

The device fabrication process includes multiple steps. Firstly, two strips of monolayer graphene are mechanically exfoliated onto the 300-nm silicon oxide substrate. The distance between the two strips of graphene defines the channel length of field-effect transistors as they are used as the contact electrodes in the next step. The direct contact of graphene upper surface is very essential as it would avoid the polymeric residues in the lithography/etching processes, which is impossible to remove and adversely impact the performances of the MoS_2 devices. In the second step, the mechanically exfoliated MoS_2 are picked up by a PPC/PMMA/PDMS stack from the silicon oxide wafer for aligned transfer. Next, the MoS_2 stripe is aligned onto the graphene electrodes, forming a residue free interface. Finally, Cr/Au (10 nm/ 50 nm) metal electrodes are integrated onto the graphene flakes with the standard e-beam lithography and metal deposition and lift-off processes. As the graphene and metal would form Ohmic contact, the final contact to the MoS_2 would also be Ohmic. The final device structure is shown in the Figure 2.1a and Figure 2.1b. A cross-sectional sample was prepared with the same method by Focused Ion Beam (FIB) and characterized using TF20 TEM. As illustrated in the TEM cross-section image (Figure 2.1c), the interface is atomically sharp and ultraclean, leading to a good van der Waals interaction between MoS_2 and graphene. Moreover, this would minimize the defects and the trapping sites at the interface.

Electrical transport

The D.C. electrical transport studies were conducted with a probe station connected to a computer-controlled analogue-to-digital converter at room temperature in vacuum under dark environment. Temperature dependent measurements were conducted with Quantum Design physical properties measurement system (PPMS). Figure 2.2a and Figure 2.2e respectively show the standard I-V output characteristic at room temperature for monolayer and multi-layers MoS_2 (with the aspect ratio W/L~1). The MoS_2 devices of different thicknesses exhibit linear I-V output characteristic without any post annealing process. Furthermore, the devices keep Ohmic behaviour with decreasing temperature down to 1.9 K (Figure 2.2b, 2.2f), suggesting that the graphene/MoS_2 contact is barrier free and the carrier can flow through the contact transparently. This behaviour can be observed in all the samples. As far as I know, the Ohmic contact at this low temperature was never achieved in previous researches. The best approach in the previous literatures is utilizing Ti as contact metal with post annealing at high-temperature in the vacuum[18], while an obvious nonlinear I-V output is still observed at a temperature of 5 K. The excellent contact in the graphene contacted MoS_2 devices can be attributed to two reasons. First, due to the limited density of state in the vicinity of Dirac cone and the unique linear dispersion relationship, the Fermi level of graphene could be easily shifted by gate doping, forming a perfect band match with MoS_2[21, 22]. The tuneable work function of graphene therefore adaptively provides excellent band match, resulting in barrier free contact with MoS_2. Moreover, the graphene strips are located underneath MoS_2 flake

and used as back contact, which could enable direct control of graphene's Fermi level with back gate voltage. For example, with 80V gate voltage applied, the work function of graphene could shift up to ~4.1 eV[23], which is significantly lower than the electron affinity of MoS_2 (~4.2 eV) [24]. Compared with previous research using graphene electrodes on top of MoS_2, the bottom graphene contact brings some more difficulties into the fabrication processes. However, the device structure with back graphene electrodes shows barrier free behaviour, in contrast to the obvious barrier behaviour of MoS_2 device using graphene electrodes on top[25-28]. The difference in the contact barrier behaviour may come from the fact that gate electrical field can be screened by the electron gas in the MoS_2 [29], reducing the electrostatic control of the graphene Fermi level by the back gate. Secondly, compared with conventional metal contacted MoS_2 system, our integration protocol does not involve E-beam lithography and metal deposition process on top of MoS2 contact area, which avoid the damage to MoS_2 and polymeric residue. Unlike metals, graphene is highly inert and stable, meaning the atomic diffusion or reaction with MoS_2 is impossible[15, 30]. This non-damage van der Waals bonding provide an atomically sharp and ultraclean interface between graphene and MoS_2. Both reasons stated above minimize the density of defects and charge trapping sites, further eliminating the Fermi level pinning, which dominate the contact behaviour in metal-MoS2 system[12, 15].

The transfer characteristics of the MoS_2 devices are examined under different temperature. In the Figure 2.3, the temperature-dependent transfer curves of

monolayer MoS_2 are illustrated and the corresponding temperature-dependent conductivities is plotted in the Figure 2.3d, providing useful transport information regarding the device. Particularly, the metallic transport state and insulating transport state can be differentiated, providing a means to probe mobility limiting scattering mechanisms.

An insulating behavior (σ decrease with T) persists until V_g~50V. By increasing gate voltage to a larger value, the conductance is found to increase with temperature decreasing, indicating monolayer MoS_2 enters a metallic state. These observations, metal-insulator transition (MIT), has been studied before in the MoS_2 and my systems shows a consistent critical conductivity $\sigma \sim e^2/h$ with previous observations for monolayer MoS2 and theoretical expectations[18, 20].

Benefit from the barrier free contact, the metal insulator transition in observed on 2-terminal FETs, while in the previous reports similar behavior was observed on four terminals measurement to exclude large contact resistance in the low temperature regime. Similarly, the MIT is also observed in the multi-layer MoS_2 devices, as shown in Figure 2.3g and Figure 2.3h, while the critical gate voltage decreases to approximately 20 V. This decrease may originate from the fact that thicker MoS_2 has larger carrier concentration and smaller band gap (1.2 eV compared to the 1.8 eV for monolayer), leading to an easier transition into metallic state.

Carrier scattering mechanism

To further analyze the transport behavior of MoS_2 devices, I extract the two-terminal extrinsic FET mobility from transconductance using equations $\mu=[dI_{ds}/dV_{bg}] \times [L/(WC_iV_{ds})]$, where L /W is the ratio between channel length and width (~between 0.5 to 2 in all devices in Figure 2.3 a-c) and $C_i = 1.15 \times 10^{-8}$ F cm^{-2} is the capacitance between the MoS_2 channel and the 300-nm silicon oxide gate per unit area. By plotting the field-effect mobility of three devices plotted as a function of temperature in Figure 2.4a, further insight into the charge scattering mechanism is gained. In both monolayer device and multilayer devices, the mobility increases with decreasing temperature. The mobility can be fitted to the expression $\mu \sim T^{-\gamma}$ temperature range from 100K to 300K, with the exponent γ around 1.1 for monolayer device and 2.3 for multi-layer device, indicating the mobility is limited by in the phonon. Generally, a power law dependence with a positive exponent is indicative of a phonon scattering mechanism, which is consistent with band-like transport that is observed in some other materials such as graphene[31], Bi_2Te_3[32] and other layered material[33]. The theoretical prediction for the exponent γ is 1.52 for monolayer and 2.6 for bulk, which is consistent with the experimental results obtained in the graphene contacted MoS_2 device. Besides, I would like to mention that the graphene-contacted samples have closer values compared with the metal-MoS_2 systems reported in previous studies and the reason lies in the elimination of contact Schottky barrier. The difference between the experimental measurement results and the theoretical prediction might come the from substrate polar optical phonons, which is another effect considered in the

theoretical model. Keeping decreasing the temperature from 100 K to 50 K, both devices has their mobility dropping due to the impurity scattering, which is predicted in the numerical calculation as well and consistent with previous measurements. In the temperature regime below 50 K, the mobility becomes saturated against temperature, indicating a balance between increasing impurity scattering and decreasing phonon scattering.

Device optimization with Boron Nitride encapsulation

To further optimize device performance, Boron Nitride (BN) is used to encapsulate MoS_2 channel material. Due to the weak van der Waals interaction and missing lattice mismatch between MoS_2 and BN, the encapsulation would significantly enhance the device performance. To integrate BN layer into the existing MoS_2 device, the BN flake is transferred onto the MoS_2 device by the dry transfer technique, where no polymer residue left in the van der Waals stacking process. The temperature-dependent mobility of device with only top stacking BN layer is illustrated in the Figure 2.3b. Similarly, as shown in Figure 2.3a, the multi-layer devices behave in a similar trend with a slightly different γ in the high temperature regime, while in the low temperature regime the mobility of monolayer device keep increasing with decreasing temperature with so saturation point. This indicates that the BN encapsulation layers greatly suppress the dominant impurity scattering in the low temperature. With decreasing phonon scattering with lower temperature, the

device mobility keeps increasing. However, this monotonic increasing phenomenon is not found in top BN covered multilayer device, where the mobility still decreases after a peak around 80 K. This can be explained by the larger impurity concentration exist inside MoS_2 interlayers and could not be suppressed by top surface BN encapsulation. In terms of carrier mobility, the mobility overall increase ~120% for monolayer and ~30% for multi-layers compared with no BN encapsulation. The multilayer device has much smaller improve because the existence of top MoS_2 layer already acts as a screening layer for the bottom MoS_2 layer, which contribute most to the electronic transport. Besides, the top layer would also protect the bottom layer from the extrinsic scattering centers, resulting less effect for top BN integration. Furthermore, both bottom and top BN are also used to encapsulate device as a sandwich structure. Further improvement is observed for device mobility, as shown in Figure 2.3c, indicating that polar optical phonons from the underlying oxide may also play a role in the overall scattering at these temperatures. I would like to note the MoS_2 flake in this BN/MoS_2/BN sandwich structure could only be contacted by using graphene as electrode due to its atomic thickness, further highlighting the significance of the graphene electrodes architecture.

In order to approach the intrinsic field effect mobility, the impact of contact resistance should be further reduced. For such purpose, a long channel device with high L/W ratio (35/1.7 μm) using BN/MoS_2/graphene/BN sandwiched structure. With higher L/W ratio, the contact resistance would play less significant roles in the transport. The

device schematics is shown in Figure 2.4a. Figure 2.4b, c show the high L/W ratio MoS2 before being picked up by the BN van der Waals stack and the final architecture, respectively. The transfer characteristic versus different temperature is plotted in Figure 2.4d, which shows that the current rises rapidly with the decreasing temperature, where the I_{on} at 1.9 K is 1300% as large as I_{on} at 300 K. Compared to regular device geometry (W/L~1), the larger temperature modulation $I_{1.9\,K}/I_{300\,K}$ here strongly indicate less contribution of contact resistance to the mobility measurement. Using the same equation used before, the field effect mobility can be extracted from Figure 2.4d. The mobility versus temperature of the device is plotted in Figure 2.4e. It is obvious that the two-terminal extrinsic mobility can go up to 1300 cm^2 / V s at 1.9 K, which is a record high extrinsic field effect mobility of MoS_2 field effect transistor.

Conclusions

In summary, graphene can act as a work function adaptable electrode to the two-dimensional semiconductor materials. By using graphene as the contact material to MoS_2 transistor, barrier free contact can be achieved. It is found that the graphene can perfectly match the electronic band structure of MoS_2 leading to the Ohmic I-V output behavior in all temperature range from 300 K to 1.9 K, which cannot be achieved before using metal contact methods. Due to the Ohmic contact and the transparent transport of electrons across the interface, the metal-insulator-transition can also be observed in the two terminal devices.

Furthermore, device performance optimizations were carried out, such as encapsulation by only top BN and both sides BN, enabling BN/MoS_2/BN sandwich structure with graphene atomically thin contact. Finally, a long channel device sandwiched by born nitride (BN) was fabricated. The long channel device demonstrates significantly better performance with record high extrinsic field effect mobility over 1300 cm^2/ V s. I believe the graphene electrode contact engineering methods, as well as the device architecture and the high performance could shed light on the future electronics and open a new way for low temperature quantum transport measurement of MoS_2 and other 2D materials.

Figures

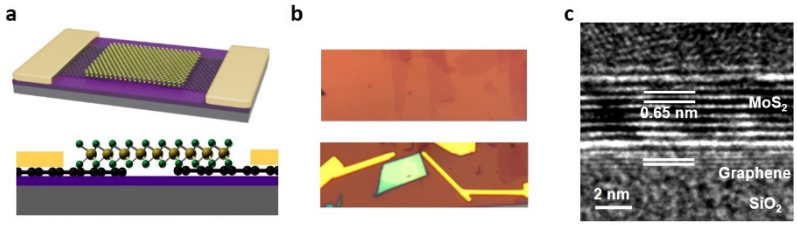

Figure 2.1 Device architecture and characterization of MoS2 transistor. (a), Perspective and cross-section view of MoS_2 device structure with graphene electrodes. (b), Top view optical image of graphene electrode and the final device structure. Graphene is highlight by dash line. (c), TEM cross-sectional image of the graphene MoS_2 interface, indicating the ultraclean and atomically sharp interface formed by the dry transfer technique.

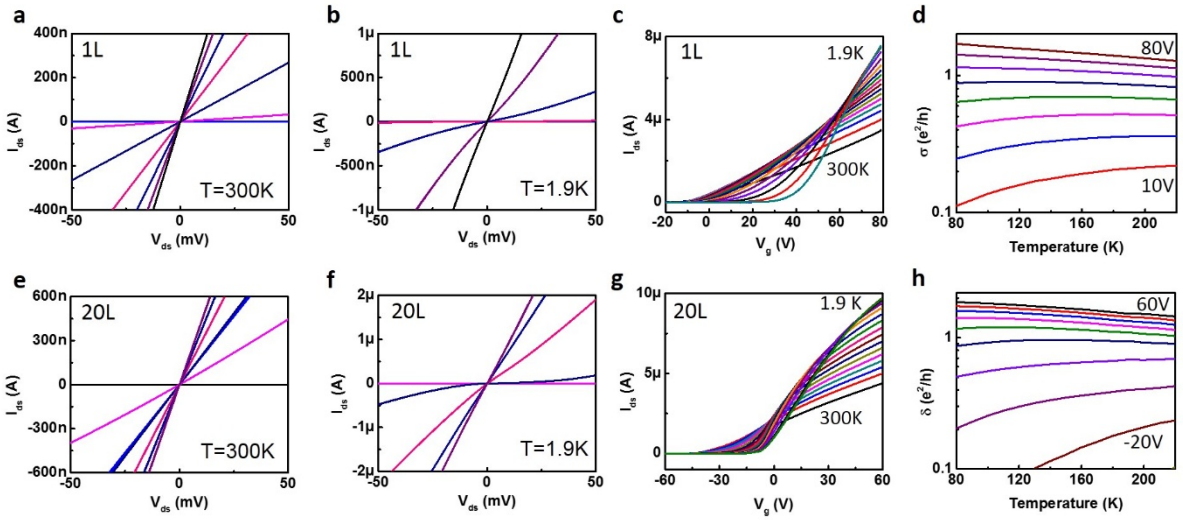

Figure 2.2 Output characteristic and transfer behavior of monolayer device and multi-layer MoS_2 device. (a, b), Output characteristic of monolayer MoS_2 device at room temperature (a) and low temperature 1.9 K (b). Ohmic I-V behavior is observed in both cases. Gate voltage is from -60 V to 80 V with 20 V as a step. (c), Transfer characteristic of monolayer device shown in a, b, with various temperature (300 K to 1.9 K, 20 K step). V_{ds} is 100 mV. (d), The conductance of monolayer device shown in a, b, c, with various temperature (10 V to 80 V, 10V step). (e, f), Output characteristic of monolayer MoS_2 device at room temperature (e) and low temperature 1.9 K (f). Linear I-V behavior is observed in both cases. Gate voltage is from -60 V to 80 V with 20 V as a step. (g), Transfer characteristic of monolayer device shown in e, f, with various temperature (300 K to 1.9 K, 20 K step). V_{ds} is 100 mV. (h), The conductance of monolayer device shown in e, f, g, with various temperature (10 V to 80 V, 10V step).

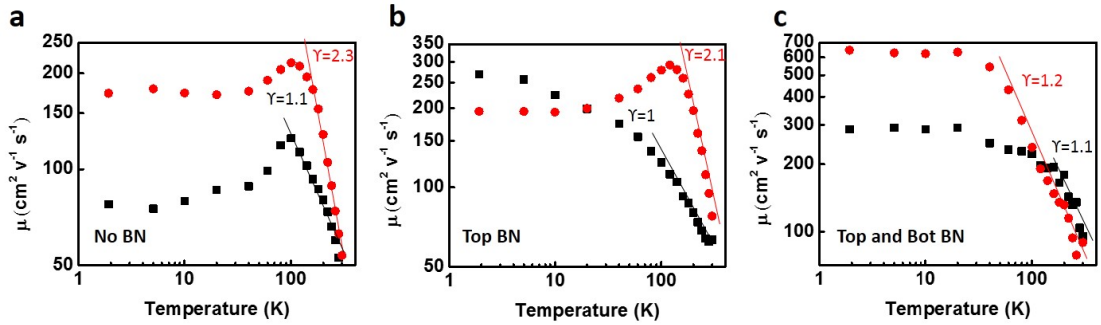

Figure 2.3 Mobility engineering of MoS_2 transistor by BN encapsulation. (a), Extrinsic field effect mobility for monolayer and multilayer devices versus various temperature (300 K to 1.9 K), linear fitting is used in phonon control region (100 K to 300 K) to extract γ. Monolayer device is demonstrated in black and multilayer device is in red. (b), Extrinsic field effect mobility for monolayer and multilayer devices under various temperature with top BN encapsulation. Monolayer device is black line and multilayer device is red line. (c), Extrinsic field effect mobility for monolayer and multilayer devices under various temperature with bottom and top BN encapsulation, forming a BN/graphene/BN sandwich structure. Monolayer device is demonstrated in black and multilayer device is in red.

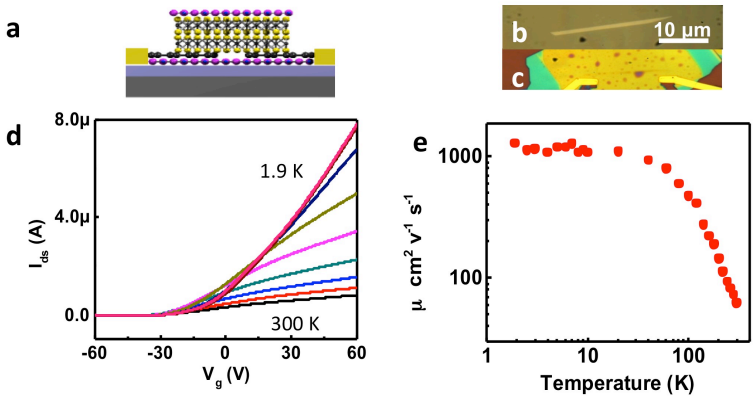

Figure 2.4 Long channel sandwiched device (a), Schematics of BN/ graphene/ MoS_2/

BN sandwiched structure with edge graphene contact. (b), Optical image of the MoS_2 flake. (c), Device image after fabrication of edge contact. (d), Transfer characteristic of device shown in c, large $I_{1.9K}/I_{300\ K}$ can be observed in this device. (e), Extrinsic field effect mobility of the device shown in e as a function of temperature, with record-high mobility over 1300 $cm^2/$ V s.

References

(1) Yoon, Y.; Ganapathi, K.; Salahuddin, S. *Nano letters* **2011,** 11, (9), 3768-3773.

(2) Radisavljevic, B.; Radenovic, A.; Brivio, J.; Giacometti, V.; Kis, A. *Nature nanotechnology* **2011,** 6, (3), 147-150.

(3) Liu, H.; Neal, A. T.; Ye, P. D. *ACS nano* **2012,** 6, (10), 8563-8569.

(4) Splendiani, A.; Sun, L.; Zhang, Y.; Li, T.; Kim, J.; Chim, C.-Y.; Galli, G.; Wang, F. *Nano letters* **2010,** 10, (4), 1271-1275.

(5) Yu, W. J.; Liu, Y.; Zhou, H.; Yin, A.; Li, Z.; Huang, Y.; Duan, X. *Nature nanotechnology* **2013,** 8, (12), 952-958.

(6) Geim, A.; Grigorieva, I. *Nature* **2013,** 499, (7459), 419-425.

(7) Britnell, L.; Ribeiro, R.; Eckmann, A.; Jalil, R.; Belle, B.; Mishchenko, A.; Kim, Y.-J.; Gorbachev, R.; Georgiou, T.; Morozov, S. *Science* **2013,** 340, (6138), 1311-1314.

(8) Cheng, R.; Jiang, S.; Chen, Y.; Liu, Y.; Weiss, N.; Cheng, H.-C.; Wu, H.; Huang, Y.; Duan, X. *Nature communications* **2014,** 5.

(9) Fiori, G.; Bonaccorso, F.; Iannaccone, G.; Palacios, T.; Neumaier, D.; Seabaugh, A.; Banerjee, S. K.; Colombo, L. *Nature nanotechnology* **2014,** 9, (10), 768-779.

(10) Liu, H.; Ye, P. D. *Electron Device Letters, IEEE* **2012,** 33, (4), 546-548.

(11) Yin, Z.; Li, H.; Li, H.; Jiang, L.; Shi, Y.; Sun, Y.; Lu, G.; Zhang, Q.; Chen, X.; Zhang, H. *ACS nano* **2011,** 6, (1), 74-80.

(12) Das, S.; Chen, H.-Y.; Penumatcha, A. V.; Appenzeller, J. *Nano letters* **2012,** 13, (1), 100-105.

(13) Chen, J.-R.; Odenthal, P. M.; Swartz, A. G.; Floyd, G. C.; Wen, H.; Luo, K. Y.; Kawakami, R. K. *Nano letters* **2013,** 13, (7), 3106-3110.

(14) Jariwala, D.; Sangwan, V. K.; Late, D. J.; Johns, J. E.; Dravid, V. P.; Marks, T. J.; Lauhon, L. J.; Hersam, M. C. *Applied Physics Letters* **2013,** 102, (17), 173107.

(15) McDonnell, S.; Addou, R.; Buie, C.; Wallace, R. M.; Hinkle, C. L. *ACS nano* **2014,** 8, (3), 2880-2888.

(16) Kaushik, N.; Nipane, A.; Basheer, F.; Dubey, S.; Grover, S.; Deshmukh, M. M.; Lodha, S. *Applied Physics Letters* **2014,** 105, (11), 113505.

(17) Dankert, A.; Langouche, L.; Kamalakar, M. V.; Dash, S. P. *ACS nano* **2014,** 8, (1), 476-482.

(18) Baugher, B. W.; Churchill, H. O.; Yang, Y.; Jarillo-Herrero, P. *Nano letters* **2013,** 13, (9), 4212-4216.

(19) Bao, W.; Cai, X.; Kim, D.; Sridhara, K.; Fuhrer, M. S. *Applied Physics Letters* **2013,** 102, (4), 042104.

(20) Radisavljevic, B.; Kis, A. *Nature materials* **2013,** 12, (9), 815-820.

(21) Yu, W. J.; Li, Z.; Zhou, H.; Chen, Y.; Wang, Y.; Huang, Y.; Duan, X. *Nature materials* **2013,** 12, (3), 246-252.

(22) Liu, Y.; Zhou, H.; Cheng, R.; Yu, W.; Huang, Y.; Duan, X. *Nano letters* **2014,** 14, (3), 1413-1418.

(23) Zhang, Y.; Tan, Y.-W.; Stormer, H. L.; Kim, P. *Nature* **2005,** 438, (7065), 201-204.

(24) Choi, M. S.; Lee, G.-H.; Yu, Y.-J.; Lee, D.-Y.; Lee, S. H.; Kim, P.; Hone, J.; Yoo,

W. J. *Nature communications* **2013,** 4, 1624.

(25) Kwak, J. Y.; Hwang, J.; Calderon, B.; Alsalman, H.; Munoz, N.; Schutter, B.; Spencer, M. G. *Nano letters* **2014,** 14, (8), 4511-4516.

(26) Yoon, J.; Park, W.; Bae, G. Y.; Kim, Y.; Jang, H. S.; Hyun, Y.; Lim, S. K.; Kahng, Y. H.; Hong, W. K.; Lee, B. H. *Small* **2013,** 9, (19), 3295-3300.

(27) Yu, L.; Lee, Y.-H.; Ling, X.; Santos, E. J.; Shin, Y. C.; Lin, Y.; Dubey, M.; Kaxiras, E.; Kong, J.; Wang, H. *Nano letters* **2014**.

(28) Roy, T.; Tosun, M.; Kang, J. S.; Sachid, A. B.; Desai, S.; Hettick, M.; Hu, C. C.; Javey, A. *ACS nano* **2014**.

(29) Castellanos-Gomez, A.; Cappelluti, E.; Roldán, R.; Agraït, N.; Guinea, F.; Rubio-Bollinger, G. *Advanced Materials* **2013,** 25, (6), 899-903.

(30) Mönch, W. *Applied physics letters* **1998,** 72, (15), 1899-1901.

(31) Chen, J.-H.; Jang, C.; Xiao, S.; Ishigami, M.; Fuhrer, M. S. *Nature nanotechnology* **2008,** 3, (4), 206-209.

(32) Steinberg, H.; Gardner, D. R.; Lee, Y. S.; Jarillo-Herrero, P. *Nano letters* **2010,** 10, (12), 5032-5036.

(33) Larentis, S.; Fallahazad, B.; Tutuc, E. *Applied Physics Letters* **2012,** 101, (22), 223104.

Chapter 3 Theoretical analysis of graphene/ MoS_2 heterostructure

Introduction

In the Chapter 2, the graphene contact has been demonstrated as a protocol to achieve barrier-free contact to the MoS_2 transistors. The reason is attributed to the doping of graphene by the adjacent MoS_2. The doping increases or decreases the Fermi level position of graphene accordingly, making graphene an adaptable contact to the semiconductor channel materials.

Derivation of equations of monolayer graphene/ MoS_2 heterostructure.

We start from Poisson's equation in semiconductor:

$$\frac{d^2\varphi_i}{dx^2} = -\frac{q}{\epsilon}(N_D^+ + p - N_A^- - n) \quad (1)$$

where φ_i is the electric potential in the system, ϵ is the dielectric constant of the material that we are considering. N_D^+ and N_A^- are the ionized donor and acceptor concentration in the semiconductor, n and p are the concentration of electron and hole, respectively. The right side of the equation represents the net charge concentration in the semiconductor.

For the MoS_2:

$$\frac{d^2\varphi_i}{dx^2} = -\frac{q}{\epsilon_{MoS_2,\parallel}}(N_D^+ - n) = -\frac{qN_D^+}{\epsilon_{MoS_2,\parallel}}(1 - e^{\beta(\varphi_i - \varphi_{i,\infty})}) \quad (2)$$

where $\epsilon_{MoS_2,\parallel}$ is the intralayer dielectric constant of MoS_2 and $\epsilon_{MoS_2,\parallel} = 15.6$[1], $\varphi_{i,\infty}$ is the potential corresponding to intrinsic Fermi energy of MoS_2 sufficiently far from the graphene/MoS_2 interface, $\beta = \frac{q}{kT}$, notation $\parallel$ represents the direction

parallel to the MoS_2/graphene interface. Compared to the equation (1), equation (2) neglect the term $p - N_A^-$ due to the fact that natural MoS_2 is intrinsically n type semiconductor due to the sulfur vacancies.

In order to solve the differential equation, multiply $d\varphi_i$ on the left and right sides of equation (2) and integrate both parts in the range of $[\varphi_{i,\infty}, \varphi_i]$:

$$(\frac{d\varphi_i}{dx})^2 = -\frac{2qN_D^+}{\epsilon_{MoS_2,\parallel}}\{(\varphi_i - \varphi_{i,\infty}) - \frac{1}{\beta}[e^{\beta(\varphi_i - \varphi_{i,\infty})} - 1]\} \quad (3)$$

Assuming the device reaches electrostatic equilibrium in the contact region or the region far from the junction interface, $\varphi_{i,\infty}$ could be set as zero. Therefore, the equation (3) is simplified as:

$$(\frac{d\varphi_i}{dx})^2_{MoS_2} = -\frac{2qN_D^+}{\epsilon_{MoS_2,\parallel}}[\varphi_i - \frac{1}{\beta}(e^{\beta\varphi_i} - 1)] \quad (4)$$

Similarly, equation (1) can also be applied to graphene. As mentioned in the Chapter 2, graphene has a finite density of states near the Dirac cone and the Fermi level position is sensitive to the doping of adjacent materials. It is necessary to replace the constant carrier concentration with a function depending on the Fermi level.

The relationship between carrier concentration and Fermi energy of graphene can be represented as[2,3]

$$E_F = \hbar v_F \sqrt{\pi |n - n_0|} \quad (5)$$

where $\hbar$ is the reduced Planck constant, v_F $(= 1\times10^6 m/s)$ is the Fermi velocity of electron[3], n is the face concentration and n_0 is the residual concentration of electron in graphene.

Plug the equation (5) into equation (1) and the result is:

$$(\frac{d\varphi_i}{dx})^2_g = \frac{-2q^3}{3\pi\,\epsilon_g\, v_F^2\, \hbar^2\, d}(\varphi_F - \varphi_i)^3 \quad (6)$$

$\in_g$ $(= 2.4)$[3] is the dielectric constant of graphene and d ($\approx$ 0.34 nm)[5] is the monolayer graphene thickness.

At the interface of MoS_2 and graphene, the boundary condition of electric field can be utilized. In other word, the normal component of electric displacement vector should be continuous across the graphene/MoS_2 interface.

$$\in_g \left(\frac{d\varphi_i}{dx}\right)_{graphene} = \in_{MoS_2,\perp} \left(\frac{d\varphi_i}{dx}\right)_{MoS_2} \quad (7)$$

where $\in_{MoS_2,\perp}$ $(= 6.34)$[1] is interlayer dielectric constant of MoS_2, and $\perp$ notation represents the direction perpendicular to the interface.

Combining equation (4), (5) and (7), an equation for numerical solution can be obtained:

$$-\in^2_{MoS_2,\perp} \frac{2qN_D^+}{\in_{MoS_{2,\parallel}}} [\varphi_i - \frac{1}{\beta}(e^{\beta\varphi_i} - 1)] = -\in_g^2 \frac{2q^3 N_{D,g}^+}{3\pi \in_g v_F^2 \hbar^2 d} (\varphi_F - \varphi_i)^3 \quad (8)$$

As illustrated in Figure 3.1, φ_F is related to the work function of graphene, electron affinity of MoS_2, and the distance from Fermi level to conduction band.

From the geometric relation in Figure 3.1, the band bending of graphene is equal to the length of AB, therefore:

$\varphi_F = AB = \frac{\phi_g - \chi_{MoS_2} - \Delta E}{-q}$ where ΔE can be calculated using effective density of states $N_c = 8\times10^{12} cm^{-2}$.[6]

Derivation of equations of bilayer graphene/ MoS_2 heterostructure.

The bilayer MoS_2/graphene system is analogous to the monolayer MoS_2/graphene system except that in bilayer graphene case, the Fermi energy is related to carrier concentration in another form[7]:

$$E_F = \frac{\hbar^2 \pi |n - n_0|}{2m^*} \tag{9}$$

where $m^* = 0.033 m_e$ is the effective mass of electron in bilayer graphene[7,8]. By a similar derivation procedure to that of monolayer graphene, equation (10) can be obtained:

$$\left(\frac{d\varphi_i}{dx}\right)_g^2 = \frac{2q^2 m^*}{\pi \in_g \hbar^2 d} (\varphi_F - \varphi_i)^2 \tag{10}$$

Combining equation (4) (7) (10), the equation for numerical calculation is acquired:

$$A(\varphi_F - \varphi_i)^2 = \varphi_i - \frac{1}{\beta}(e^{\beta \varphi_i} - 1) \tag{11}$$

where $A = \frac{-\in_g \in_{MoS_{2,\parallel}} m^* q}{\pi \in^2_{MoS_{2,\perp}} \hbar^2 d N_D^+}$.

Derivation of equations of multilayer graphene/ MoS_2 heterostructure.

Similarly, in order to solve the equation for numerical calculation for multilayer graphene/MoS_2 junction, we start from the E-k relation of multilayer graphene[9]:

$$E_k = t_\perp cos\left(\frac{\pi n}{N+1}\right) \pm \sqrt{(v_F|k|)^2 + t_\perp^2 cos^2\left(\frac{\pi n}{N+1}\right)} \tag{12}$$

where $t_\perp$ is the hopping energy between two adjacent carbon atoms, and we take $t_\perp = 0.3eV$[9]. The $\pm$ represents the conduction band and valence band of the graphene layer respectively.

In graphene system whose layer number N is larger than three, the carrier concentration as a function of Fermi level can be derived from (16). In other word, the total density of states can be obtained by adding up the density of states in individual layer of the graphene stacks. When the layer number is odd ($N = 2m + 1, m = 1,2, \ldots\ldots$), the carrier concentration can be represented as

$$n = \frac{1}{\pi}\hbar^{-2}{v_F}^{-2}[\frac{m+1}{2}\left(\Delta E_f\right)^2 - t_\perp \Delta E_f \sum_{n=m+1}^{2m+1} \cos\left(\frac{n\pi}{2m+2}\right)] \quad (13)$$

While for even number layered graphene stacks ($N = 2m, m = 1, 2, \ldots\ldots$), the carrier concentration becomes:

$$n = \frac{1}{\pi}\hbar^{-2}{v_F}^{-2}[\frac{m}{2}\left(\Delta E_f\right)^2 - t_\perp \Delta E_f \sum_{n=m}^{2m} \cos\left(\frac{n\pi}{2m+1}\right)] \quad (14)$$

Utilizing same solution method for monolayer graphene and bilayer graphene, we can derive the equation for numerical calculations:

$$A(\varphi_F - \varphi_i)^3 + B(\varphi_F - \varphi_i)^2 = \varphi_i - \frac{1}{\beta}(e^{\beta\varphi_i} - 1)$$

For odd layer numbers,

$$A = \frac{q^2 \epsilon_g \in_{MoS_{2,\parallel}} (m+1)}{6\pi\hbar^2 \in^2_{MoS_{2,\perp}} v_F^2\, d\, N_D^+},\ \mathrm{B} = \frac{q\epsilon_g \in_{MoS_{2,\parallel}} t_\perp}{2\pi\hbar^2 \in^2_{MoS_{2,\perp}} v_F^2\, d\, N_D^+} \sum_{n=m+1}^{2m+1} \cos\left(\frac{n\pi}{2m+2}\right) \quad (15)$$

For even layer numbers,

$$A = \frac{q^2 \epsilon_g \in_{MoS_{2,\parallel}} m}{6\pi\hbar^2 \in^2_{MoS_{2,\perp}} v_F^2\, d\, N_D^+},\ \mathrm{B} = \frac{q\epsilon_g \in_{MoS_{2,\parallel}} t_\perp}{2\pi\hbar^2 \in^2_{MoS_{2,\perp}} v_F^2\, d\, N_D^+} \sum_{n=m}^{2m} \cos\left(\frac{n\pi}{2m+1}\right). \quad (16)$$

Barrier lowering effect induced by image charge

Apart from the doping effect, we further considered the barrier reduction due to image force effect on graphene/MoS_2 interface. The barrier reduction due to image force effect is $\Delta\phi = \sqrt{\frac{q|\frac{d\varphi_i}{dx}|}{4\pi\epsilon_s}}$, where ϵ_s is the dielectric constant of MoS_2 and $\frac{d\varphi_i}{dx}$ is the

electric field at the interface[10]. $\frac{d\varphi_i}{dx}$ at the interface can be deduced from the values of φ_i calculated by numerical method. With the image force effect correction, the barrier at the interface of MoS_2/graphene can be further lowered.

Simulation results of the MoS2/graphene contact barrier

In order to quantify the MoS_2/graphene contact barrier, the mathematical models are implemented in Python. A binary search algorithm is utilized to find the solution of φ_i. A discrete-valued grid is meshed in the state space of φ_i in order to estimate the numerical solution and the grid density determines the solution precision. For our calculations, the solution precision is set as 0.05 meV. The simulation results are illustrated in the Figure 3.2. As shown in the Figure 3.2 (a), the graphene Fermi level shift, which indicates the doping level of graphene by the adjacent MoS_2 layer can be represented as a function of graphene stack layer and the carrier concentration of MoS_2 flake. Generally, as the MoS_2 carrier concentration increases, the Fermi level shift of graphene stacks also increases. This can be easily understood by the carrier diffusion, where more electrons in MoS_2 will diffuse into graphene layer when the carrier concentration increases. Besides, the Fermi level of graphene is also closely related to the layer of graphene stacks, which is expected in the derivation process. With increasing graphene layer number, the density of states will also rise, making the Fermi level shift less than that of thinner graphene stacks. Similarly, the Schottky barrier is dependent on the carrier concentration and graphene layer number as well.

The barrier height has the similar trends as the Fermi level shift, as shown in the Figure 3.2 (b). It can be seen that with graphene layer decreases to monolayer, the barrier height is zero even with intrinsic carrier concentration in MoS_2. Figure 3.2 (c) illustrates the barrier heights of monolayer graphene and MoS_2. The barrier height also depends on the mismatch between the initial band structures of monolayer graphene and MoS_2. Generally, the less initial mismatch of the band structures leads to smaller barrier heights because less electrons are required to dope the graphene layer.

Conclusions

In conclusion, the analytical equation of the graphene/MoS_2 is derived in this chapter. Based on the analytical equation of the interface, the barrier height can be solved numerically as a function of MoS_2 carrier concentration, graphene stack layer number and initial band mismatch. In order to achieve the zero barrier height of the graphene and MoS_2, the graphene thickness should be as thin as possible. Moreover, the smaller band mismatch and higher carrier concentration would also contribute to the elimination of Schottky barrier. The simulation results are consistent with the experimental results discussed in the Chapter 2.

Figures

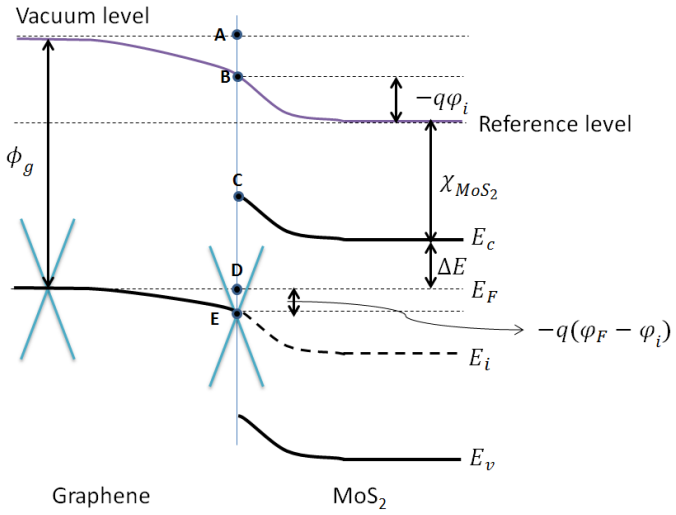

Figure 3.1. The band diagram of graphene/MoS_2 heterostructure. The left side is graphene and the right side is MoS_2. The Dirac cone of graphene is also plotted in the figure. At the interface, the segment DE represents the doping of graphene.

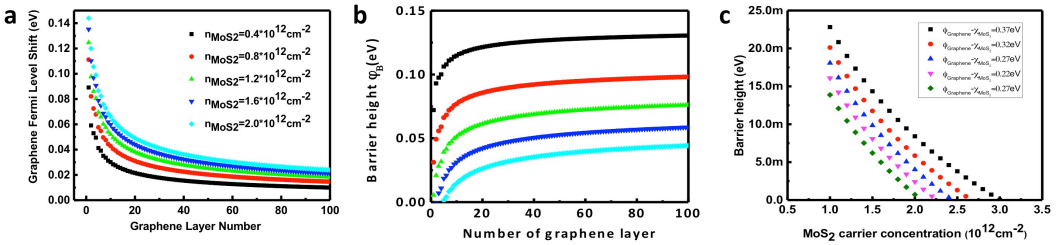

Figure 3.2 Simulation results of adaptable graphene contact (a), The graphene Fermi level shift as a function of graphene layer number and carrier concentration of MoS_2 flake. (b), The barrier height of MoS_2/graphene junction's dependence on the graphene layer number and carrier concentration of MoS_2 flake. (c), Barrier height as the function of initial band mismatch between MoS_2 and graphene.

References

1 Ataca, C., Topsakal, M., Akturk, E. & Ciraci, S. A Comparative Study of Lattice Dynamics of Three- and Two-Dimensional MoS2. *J. Phys. Chem. C* **115**, 16354-16361 (2011).

2 Zhang, Y. B., Tan, Y. W., Stormer, H. L., & Kim, P. Experimental Observation of the Quantum Hall Effect and Berry's Phase in Graphene. *Nature* **438**, 201-204 (2005).

3 Neto, A. H. C., Guinea, F., Peres, N. M. R., Novoselov, K. S. & Geim A. K. The Electronic Properties of Graphene. *Rev. Mod. Phys.* **81**, 109-62 (2009).

4 Lemme, M. C., Echtermeyer, T. J., Baus, M. & Kurz, H. A graphene field-effect device. *IEEE Electron Device Lett.* **28**, 282-284 (2007).

5 Ni, Z. H. et al. Graphene thickness determination using reflection and contrast spectroscopy. *Nano Lett.* **7**, 2758-2763 (2007).

6 Kaasbjerg, K., Thygesen, K. S. & Jacobsen, K. W. Phonon-limited mobility in n-type single-layer MoS2 from first principles. *Phys. Rev. B* **85**, 115317 (2012).

7 Yu, Y. J. et al. Tuning the Graphene Work Function by Electric Field Effect. *Nano Lett.* **9**, 3430-3434 (2009).

8 Henriksen, E. A. et al. Cyclotron resonance in bilayer graphene. *Phys. Rev. Lett.* **100**, 087403 (2008).

9 Guinea, F., Neto, A. H. C. & Peres, N. M. R. Electronic states and Landau levels in graphene stacks. *Phys. Rev. B* **73**, 245426(2006).

10 Sze, S. M. Semiconductor Devices: Physics and Technology Ch. 12 (Wiley, New

York, 1986).

Chapter 4 Directly profiling the localized states in monolayer MoS_2 with graphene contacted field effect transistor

Introduction

Two-dimensional layered materials (2DLMs) represent an exciting class of materials with many intriguing properties such as metal-insulator transition[1], superconductivity[2], and Shubnikov–de Haas oscillations[3]. Among these materials, molybdenum disulfide (MoS_2) is the most investigated n-type semiconductor with a direct bandgap of 1.8 eV for monolayers and an indirect bandgap of 1.2 eV for multilayers[4-6]. The atomically thin geometry of 2D semiconductors may promise lower power dissipation electronic devices for integrated circuits[7-9], and the direct bandgap monolayer materials have generated considerable interest for diverse optoelectronic applications[10-14]. However, the attained experimental field-effect mobility of MoS_2 supported on SiO_2 substrate thus far is still considerably lower than the theoretically predicted value[1,15-17], which can be largely attributed to the scattering by disorders in MoS_2 or at the substrate-MoS_2 interface[18-20].

Recent studies have demonstrated that both the encapsulation of MoS_2 in the high-k dielectrics and passivation by the boron nitride could suppress the disorders in the system, therefore leading to high mobility[1,3,16]. Additionally, the suppression of disorders also contributes to a transition into metallic states at a lower carrier

concentration[15]. In the metallic regime, the electronic transport is mainly dominated by the extended state. On the other hand, in the insulating regime, the electronic transport shows the characteristics of variable-range hopping at cryogenic temperature, indicating the presence of localized states[21-23]. Recent studies suggest that the structural disorders such as sulfur vacancies are the primary sources of localized states while the charge trap states at the SiO_2/MoS_2 interface also contribute[15]. Transmission electron microscopy (TEM)[24], scanning tunneling microscopy (STM)[25] and the capacitance measurements[26,27] have been utilized to investigate the localized states distribution, each with their own merits and drawbacks. For instance, it is impossible to obtain the electronic structure of localized states with TEM approach, while the STM measurement is merely able to resolve the electronic structure on the upper surface of the MoS_2. Capacitance measurement can resolve the electronic structure of localized states, but it is incapable of excluding the capacitance contribution from the localized states away from the multilayer MoS_2/SiO_2 interface. Moreover, the capacitance of the localized states is rather small compared to the total capacitance in the measurement configuration, thus greatly degrading the resolution of density of states (DOS) measurement[27]. Overall, these techniques are insufficient to offer direct information on the conduction along the interface[25-27], which is important for understanding the charge transport behavior and potential applications of atomically thin MoS_2.

Here we report a field-effect detection approach to directly probe the electronic structure of localized states in monolayer MoS_2. Distinct from the indirect studies described, the field-effect transport offers a robust approach to tune the carrier concentration and unambiguously probe the electronic states in conduction channel of MoS_2 and at the MoS_2/substrate interface. By applying an external gate voltage, the Fermi level can be readily tuned throughout the bandgap of MoS_2, thus the transport properties of each state in the vicinity of the Fermi level can be accessed and probed. Furthermore, this method can effectively avoid altering the intrinsic properties of MoS_2. For 2D electron gas systems, such technique has been widely utilized to study their temperature-dependent carrier concentration phase diagram[28]. In particular, Marré et al. have recently studied the localized states at the interface of $LaAlO_3/SrTiO_3$[29], and observed thermal power oscillation with varying gate voltage, which has been attributed to multiple discrete localized states in the framework of Boltzmann transport and phonon drag model. Nonetheless, Marré's study was not able to obtain the theoretically predicated periodic conductivity plateaus with the varying gate voltage due to the non-Ohmic behavior of contacts.

We also present, for the first time, the discovery of multiple conductivity plateaus in the transfer curve of MoS_2 field-effect transistors (FETs) without magnetic field. Distinct from the conventional MoS_2 FET with metal contacts, our MoS_2 samples were contacted with monolayer graphene as the source-drain electrodes, which

enables barrier-free contacts and allows the direct probing the localized states with small excitation voltage ($V_{ds} \leq 0.5$ mV). By combining the transport measurements and the variable-range hopping model, we achieve a very high resolution (up to 1 meV) profiling of localized states in monolayer MoS_2. The findings provide important insight into the fundamental transport properties of MoS_2 and potentially offer the strategy to improve the performances of MoS_2 devices.

Electrical transport measurements

To investigate the charge transport properties of MoS_2, field-effect transistors were constructed on a 300 nm SiO_2/Si substrate using monolayer MoS_2 flake as the semiconducting channel and two strips of monolayer graphene underneath the monolayer MoS_2 flake as the contact electrodes (Figure. 4.1 (a), inset of Figure. 1 (b)). The graphene contact to MoS_2 has been demonstrated to form an atomically abrupt interface free of Fermi level pinning, thus leading to barrier-free transparent contacts[16]. The transistor characteristics were measured in dark from 1.9 K to 300 K using Quantum Design Physical Properties Measurement System (PPMS) coupled with the Agilent B2902A Precision Source/Measure Unit. The output characteristics of monolayer MoS_2 with different gate voltages at 1.9 K show nearly perfect linear current-voltage (I_{ds}-V_{ds}) behavior (Fig. 1b), suggesting barrier-free Ohmic contacts, which are further confirmed by the temperature-dependent measurement and the positive slope in Arrhenius plotting (Figure 4.5)[16,30].

Figure 4.2 (a) illustrates the gate voltage dependence of MoS_2 sheet conductivity measured up to back gate voltage V_g = 80 V at various temperatures. The use of back gate allows effective tuning of accumulated carrier concentration up to 4.72×10^{12}/cm^2 with applied gate voltage up to 60 V at room temperature, according to gate capacitance model $n = C_{ox}(V_g - V_{th})$ [31], where n is the accumulated carrier concentration induced by gate capacitance, C_{ox} equals to 12 nF/cm^2 for the capacitance of 300 nm silicon oxide,V_g is the gate voltage and V_{th} is the threshold gate voltage. In the high carrier concentration regime at V_g > 60 V, we observed that the sheet conductivity increased with decreasing temperature, suggesting a metallic behavior of MoS_2. As previous study has revealed, this metallic behavior is related to the interplay of the electron-electron interaction and the disorders[22,28,32]. In the metallic regime, the disorders are suppressed, so the metallic state can be stabilized by the Coulomb interaction between electrons. On the other hand, when the electron concentration is below a critical value (low gate voltage < 40 V), the sheet conductivity decreases with decreasing temperature, indicating an insulating state. The divergent point between metallic state and insulating state, which was estimated around e^2/h in previous literatures[1], was also observed in our experiment. In the insulating regime, the disorders, including some extrinsic charge impurities at the MoS_2/SiO_2 interface and the intrinsic defects such as the sulfur vacancies, prevail and dominate the electron transport at low temperatures[18].

The existence of the disorders can also be proved by the temperature dependence of mobility. Figure 4.2 (b) shows the mobility of device as a function of gate voltage and temperature. The field-effect mobility is evaluated based on the equation $\mu = dI_{ds}/dV_{bg} * (L/W)/(C_{ox} * V_{ds})$, where L is the channel length, W is the channel width of MoS_2 device and C_{ox} is the normalized back-gate capacitance of silicon oxide(C_{ox} = 12 nF cm^{-2} for 300 nm SiO_2). Above 90 K, the mobility at all gate voltages keeps increasing with lowering temperature and can be fitted using the temperature-mobility relationship $\mu \sim T^{-\nu}$, where $\nu \approx 0.49 \sim 0.76$, which is in agreement with previous studies in phonon scattering governed transport in 2D electron systems in the high temperature regime[17,33-35]. On the other hand, the phonon scattering is expected to be suppressed in the low temperature regime, where the dominant scattering mechanisms are long-range charged impurity scattering and short-range neutral impurity scattering. Indeed, the mobility at a lower gate voltage (V_g<30 V) decreases with decreasing temperature in the temperature range from 90 K to 2 K (Fig. 2b). This drop indicates that the impurity scattering begins to play a more important role in the electron transport at low temperature[1,36]. However, the mobility at a higher gate voltage (V_g>30 V) does not exhibit the similar trend below 90 K. Instead, it keeps increasing and finally saturates as the temperature is approaching 2 K. The absence of the mobility decline with decreasing temperature can be attributed to the more efficient screening of Coulomb scattering potential of charged impurity at larger carrier concentration[36]. It is worth noting that the charged impurity screening

effect was also observed before in high-κ dielectric capped MoS_2 devices[1].

Figure 4.2 (b) also reveals that the mobility exhibits saturation with increasing gate voltage in the cryogenic temperature regime from 2 K to 90 K, which is consistent with previous reports[3,18]. As the back-gate voltage increases from 0 V to 30 V, the screening of long-range Coulomb scattering leads to the enhancement of mobility. When the voltage exceeds 30 V, the long-range Coulomb scattering is gradually eliminated, leaving carrier concentration-independent short-range scattering as the primary mobility limiting factor. This phenomenon has been observed and well-studied in graphene[37].

Similarly, the device also exhibits mobility saturation with increasing gate voltage in the high temperature regime (T> 90 K) and the screening of charged impurity scattering also attributes to such phenomenon. At the same time, the increasing mobility with higher carrier concentration can also be cancelled out due to an increasing phonon electron scattering rate as the characteristic energy of electron is approaching that of longitudinal optical phonon and such scattering mechanism can be described by the Fröhlich interaction[38-40]. Therefore, the overall scattering rate finally gets saturated to a certain value as the electron conduction reaches a balance between the decreasing Coulomb scattering and increasing phonon scattering.

To gain a further insight into the transport mechanism, the Arrhenius plot of sheet conductivity at different gate voltages is shown in Fig. 2c. There are clearly two distinct transport regimes. In the high temperature regime (T>30 K), the sheet conductivity σ of MoS_2 shows an exponential decrease with 1/T, which can be described as thermal activated transport[1]. In such band-like transport, carriers are thermally activated to the delocalized extended states above the mobility edge. At those extended states, the carriers can be driven by the applied electric field freely and the sheet conductivity depends mainly on the carrier concentration at the extended states. Therefore, it can be fitted with the thermally activated transport equation $\sigma = \sigma_0 exp(\frac{-E_a}{kT})$, where σ_0 is the prefactor of sheet conductivity, E_a is the thermal activation energy, k is the Boltzmann constant and T is the temperature. Using this equation, the activation energy is found to decrease with increasing carrier concentration because the Fermi level is moving closer to the mobility edge[41]. As shown in the Fig. 2d, with higher gate voltage applied to the MoS_2, the activation energy keeps decreasing from 10.4 mV to 0 mV, indicating the electrons are becoming more delocalized, consistent with the fact that localization length increases with higher carrier concentration in the percolation model[27].

Upon further decreasing temperature below 30K, the thermal activation of electron is barely possible and electrons mostly occupy the localized states below the mobility

edge rather than the extended states above the mobility edge. Therefore, the dependence of sheet conductivity on the temperature is weakened and the thermally activated transport behavior can no longer be observed. The dominating transport behavior in this regime is attributed to the variable-range hopping (VRH) and can be described as $\sigma = \sigma_0 \exp\left[-(\frac{T_0}{T})^{1/(d+1)}\right]$, where σ_0 is the sheet conductivity prefactor, T_0 is the correlation energy scale, T is the temperature and d is the dimension of the system[19,21,42]. Previous study suggested that the VRH at low temperature originated from the midgap intrinsic defect states in the MoS_2 samples and trap states at the MoS_2/SiO_2 interface[15].

To further examine the localized states in MoS_2, small bias voltage on the order of 0.1 mV was applied to the device. Distinct from the 0.1 V bias voltage applied in Fig. 2a, a small bias would not excite the electrons to the extended states above the mobility edge, therefore the electrons are most likely to migrate between the states near the Fermi level. Figure 4.3 (a) shows the transfer curves with 0.5 mV excitation voltage respectively at 2 K, 5 K, and 30 K. Importantly, these transfer curves (particularly the one at 2 K) show dramatically different features from those at high-bias-voltage (V_{ds} = 0.1 V) with notable conductivity plateaus with changing gate voltage. The first plateau spans from 22 V to 32 V along the x-axis, and as the gate voltage increases, the width of conductivity plateau gradually reduces to 5 V. Additionally, the universal conductance fluctuation patterns are also found to superimpose those plateaus. In

contrast to the wide conductivity plateaus, the universal conductance fluctuation patterns are a set of randomly distributed peaks with full width at half maximum around 1 V. The signatures of the universal conductance fluctuation are consistent with those found in other 2D electron gas systems with disorders, such as Si and graphene[43,44].

When the temperature is above 5 K, the universal conductance fluctuation patterns in the transfer curve almost completely vanish while the first conductivity plateaus still exist. Moreover, when the temperature further rises to 30 K, the conductivity plateaus completely vanish. The reasons for divergent characteristics of conductivity plateaus and universal conductance fluctuations lie in the different nature of the two transport processes. The universal conductance fluctuation is a coherent transport that is more sensitive to temperature than the phonon assisted hopping. However, the universal conductance fluctuation requires a large resonant density of states to be built up, whose process usually takes ~0.01 s in a two-dimensional electron gas system, without destructively incoherent scattering[44,45]. Nevertheless, the nature of hopping is a diffusive transport. Therefore, the disappearance of plateaus is caused by thermal broadening of conduction carrier distribution near the Fermi level. Figure 4.3 (b) illustrates the transfer curve at 5 K with different bias voltages; the positions of plateaus are independent of bias voltage. As the bias voltage determines the momentum of conductive electrons, the positions of plateaus are supposed to shift

with different bias voltages if the transport was coherent[46]. In contrast, the independence of plateau with bias voltage in our measurements indicates that the transport is dominated by the hopping process known as an incoherent transport, in which different conductive paths do not interfere with each other.

Conductivity plateaus

We have qualitatively investigated the localized-state induced conductivity plateaus, which are observed for the first time in the 2D disordered systems as far as we know. We attribute this discovery to the barrier-free Ohmic contact of MoS_2 transistors. The existence of Schottky barrier in previous MoS_2 FETs usually requires a large bias voltage to turn on the devices, therefore hindering the application of low excitation voltage that is necessary to probe these localized states near band edge. When the excitation voltage exceeds a certain value, the carrier would be pumped to the extended states with higher energy. Therefore, the transport of localized electrons is less significant and their features are covered up with the onset of band-like transport. Another important reason is that the voltage excitation would also broaden the conduction energy level in the same mechanism as temperature does[47]. Thus, when the bandwidth of conduction energy level exceeds that of discrete localized states, the signatures would fade away. In order to elucidate the contributions from the contact to the conductivity plateaus, MoS_2 FETs with 5nm/50nm Cr/Au as contacts were also fabricated. In a negligible number of devices with undetectable Schottky barrier

through the Arrhenius plots method, the similar behavior was also observed (Figure 4.5). However, most devices exhibit imperfect contacts with no conductivity plateaus observed due to the reasons stated before, which also confirms the indispensable role of transparent contact in the detection of conductivity plateaus.

To confirm the hypothesis of plateaus' origin, the sheet conductivity of MoS_2 was simulated quantitatively by using an improved variable-range hopping model including a series of discrete localized states. This model can reproduce well the conductivity plateaus and their evolutions as a function of temperature. Two-types of states, including the localized states and extended states were included in this model and the mobility edge acts as the boundary separating those two kinds of states. Below the mobility edge, the electron would hop to the most probable localized states with the assistance of a phonon; while for the transport of extended states above the mobility edge, the electrons would behave as free electrons in a band-like transport. Therefore, the transport in this model is a combination of two mechanisms, which have been proved before in chemical vapor deposited MoS_2[26]. For the electrons in the extended states, the band mobility is commonly used to represent the transport properties. It is the free electron mobility in the extended states, and is different from the measured "effective" field-effect mobility which is indeed an average value for both localized electrons and free electrons at a given carrier concentration. As it can hardly be extracted from experiment, the theoretical band mobility was used in our

model[39]. In addition, as previously described, the positions of localized states in the band diagram were estimated by the activation energy fitted from the sheet conductivity-temperature relation $\sigma = \sigma_0 exp(\frac{-E_a}{kT})$, utilizing the experimental data in the Arrhenius type transport regime (T>30 K).

The calculation of net hopping conduction was implemented by the integration of the differential sheet conductivity of each state contributing to the conduction[48]. Then, the differential sheet conductivity was obtained through a complicated function of the successful hopping attempt frequency, localized states' positions, average hopping distance, and the probability of phonon assistance. This model is consistent with the scenario that sheet conductivity depends proportionally on$1/T^{1/(1+d)}$, where T is the temperature and d is the dimension of the system. Furthermore, the distribution of localized states was obtained by inserting a series of localized states in the bandgap. Specifically, the width and DOS of the localized states were calculated by minimizing the deviation between theoretical and experimental transfer curves below 30 K. The profile of the discrete localized states was shown in the Figure. 4(a). The mobility edge is 0 meV in this diagram and the localized states are distributed in the range of -12 meV to -2 meV, which is close to the range estimated from the experiment. Additionally, by integrating the DOS, the total concentration of localized states can be estimated to be 4.52×10^{12} /cm^2, which is largely consistent with the concentration of atomic defects in previous TEM study[24]. At last, we would like to note that the profile

of those localized states is enveloped in an exponential decaying function that was widely used to describe the distribution of localized states[26]. Together with this approach, the precision of electronic structure can be pushed up to the limit of 1 meV.

The simulated and experimental transfer curves at 2 K and 30 K are illustrated in Figure 4.4(b). Significantly, the key features in the experimental data were well reproduced in the simulated curves. In the experiments, the width of conductivity plateau observed at a lower gate voltage is wider than those observed at higher gate voltage. In our theory, the reason for a narrower plateau at higher gate voltage is that the uplifted Fermi level would be closer to the mobility edge, leading to more electrons at the extended states. Therefore, the growing number of delocalized electrons covers up the features of hopping transport. In addition, the disappearance of plateau at higher temperature can also be interpreted in the framework of our model. As the bandwidth of conduction energy level near the Fermi level approximately equals to 4kT, it would be broadened as the temperature increases[49,50]. Once the width of conduction energy level exceeds that of localized states, the corresponding plateau would vanish as the results of "thermal smearing". In the case of our device, the width of each localized states in the band diagram is approximately 2 mV. Hence as the temperature reaches 6 K, the conduction energy level starts to cover the adjacent localized states. Therefore, the adjacent localized states near the Fermi level contribute to the conduction and become irresolvable, making the conduction plateaus

begin to vanish. When the temperature exceeds 30 K, the conduction energy level is wider than that of the whole localized states region, leading to the complete disappearance of conduction plateaus in the transfer curves. To verify that the conductive plateaus are induced by the localized states, a multilayer MoS_2 device was also measured and simulated with the same procedures. (Figure 4.5, Figure 4.6, Figure 4.7) The simulation results confirm the DOS of localized states in monolayer MoS_2 is higher than that in multilayer MoS_2, suggesting the monolayer MoS_2 is a more disordered system. This trend is to that obtained with capacitance measurements[27].

Conclusions

In conclusion, we have measured the electronic field-effect transport properties of MoS_2 with graphene as barrier-free contacts. The sheet conductivity and mobility versus temperature relationships reveal that the electron variable-range hopping dominates the transport property below 30 K. In the hopping transport dominated temperature range, the transfer curves with low bias voltage ($V_{ds} \leq$ 0.5 mV) display a series of conductivity plateaus, which are believed to be induced by the discrete localized states in the MoS_2 conduction channel.

This behavior was unprecedented in the previous literatures due to the non-Ohmic

behavior contact to the MoS_2. With the transparent contact of graphene, we firstly observed this behavior and the electronic structure of the localized states can be resolved within the framework of variable-range hopping model. The electronic structure of localized states can be directly characterized and the resolution of the localized states can be achieved up to 1meV, which is beyond the limit of other techniques such as capacitance measurement and photoluminescence measurement. In this regard, our method offers a general approach for directly probing the localized states and a direct evidence of the hopping transport origin.

Figures

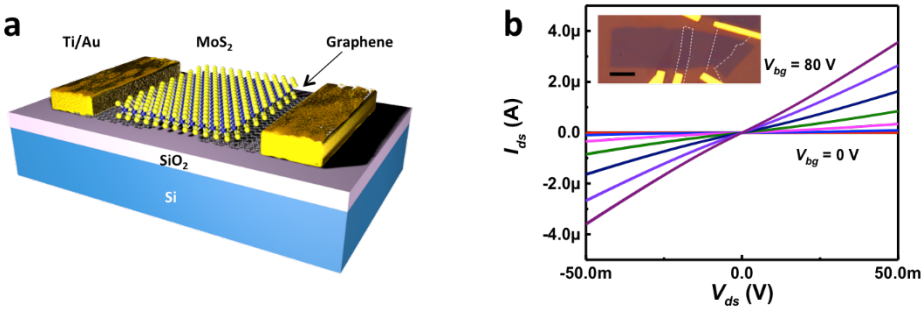

Figure 1.1 The schematic and the I_{ds}-V_{ds} output of monolayer MoS_2 device at 1.9K. (a), Schematic of a monolayer MoS_2 FET with monolayer graphene as electrodes. The picture shows that the monolayer MoS_2 as the FET channel material is contacted by monolayer graphene. The drain and source electrodes are connected to source measurement unit with Ti/Au (50nm/50nm) electrodes. (b), The I_{ds}-V_{ds} output curves of MoS_2FET with different gate voltage at 1.9K. The inset shows an optical image of

a typical monolayer MoS_2 device. The graphene electrodes are marked by white dashed lines in the image. Scale bar, 5 μm.

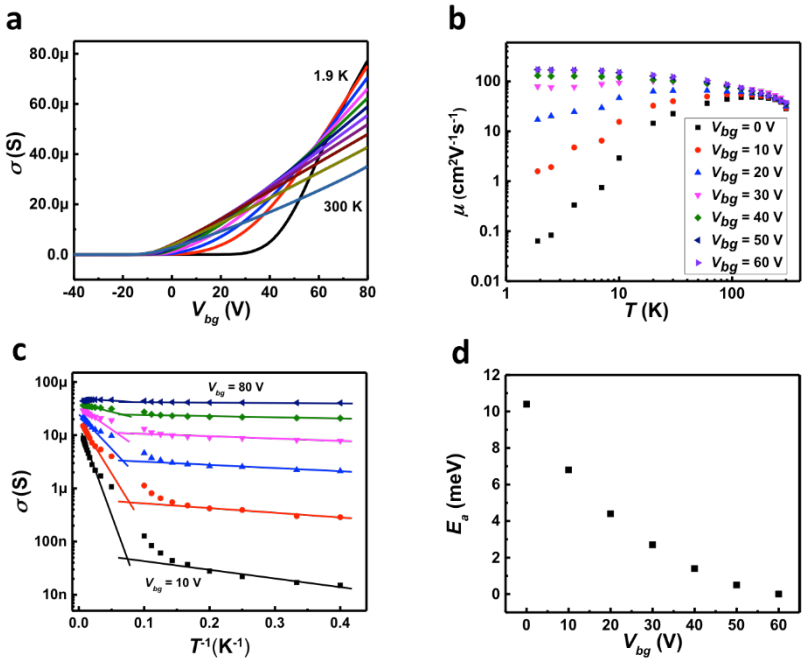

Figure 2.2 Transfer curves and temperature-dependent transport properties of MoS_2 FET. (a), The transfer curves of MoS_2FET at different temperatures from 300K to 1.9K. At lower back gate voltage below 60 V, the sheet conductivity σdecreases with decreasing temperature while as the gate voltage increases above 60V the sheet conductivity increases with decreasing temperature, indicating the transition from insulating regime to metallic regime. (b), The mobility of MoS_2 as a function of temperature at different gate voltages from 0V to 60V. (c), The Arrhenius plot of the sheet conductivity $\sigma$of monolayer MoS_2 in the insulating regime (V_{bg}< 60 V). The weakened dependence of sheet conductivity over the temperature below 30 K is

indicative of variable-range hopping dominant transport in this temperature range. (d), The activation energy E_a as a function of back gate voltage V_{bg}.

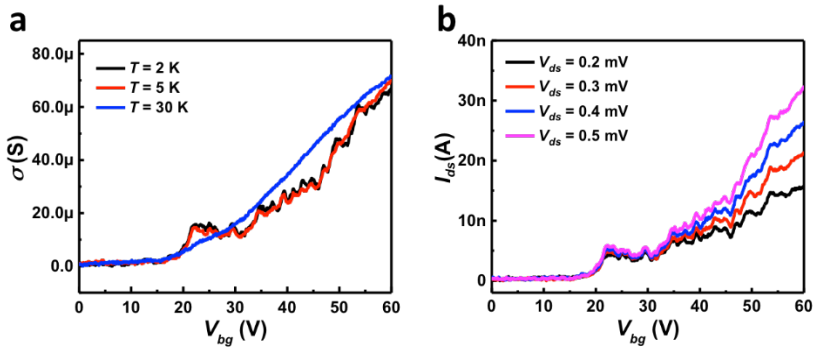

Figure 3.3 The temperature-dependent and bias voltage-independent sheet conductivity plateaus. (a), The sheet conductivity$\sigma$of MoS_2 as a function of back gate voltage V_{bg} at 2 K, 5 K, and 30 K with 0.5 mV as the excitation bias voltage. The conductivity plateaus can be clearly observed in the 2 K curves and gradually disappear when temperature increases. (b), The current plateaus at 5 K with different excitation voltage, the position of the plateaus is independent of the excitation voltage.

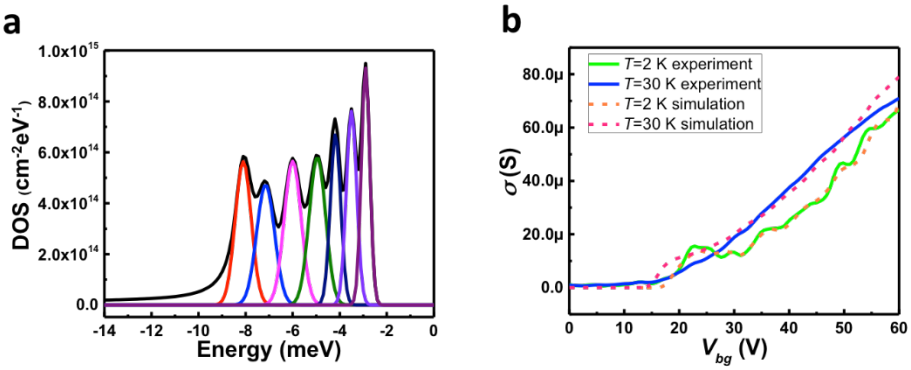

Figure 4.4 Simulated DOS of localized states and corresponding transfer curves. (a), The DOS of localized states extracted from the sheet conductivity plateau with variable-range hopping model. 0meV is the mobility edge, below which lie the regularly distributed discrete localized states. (b), The simulated transfer curves at 2 K and 30 K with the localized states in Figure. 4.4 (a) and the comparison with the corresponding experimental transfer curves.

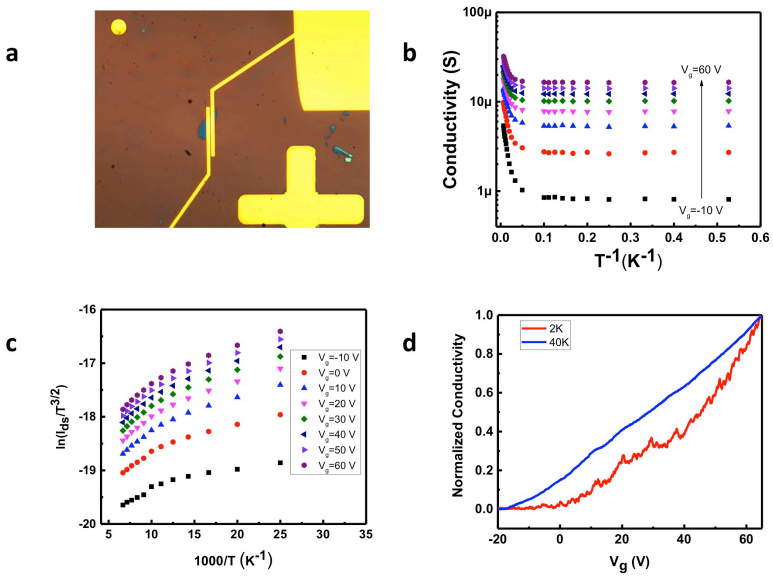

Figure 4.5 The optical image of MoS_2 device and its temperature-dependent characterization. (a), The optical microscope image of a MoS_2 sample device with metallic contact, the channel length is 300 nm. (b), The Arrhenius plot of normalized conductivity of the device in Figure 4.5 (a) and the hopping behavior. (c), The Arrhenius plot of the metal contact device, the positive slopes indicate the Schottky barrier is undetectable in the temperature-dependent conductivity measurements. (d), The normalized transfer curves with excitation of 0.5 mV source voltage at 2 K and

40 K respectively. The conductivity plateau could also be observed in the transfer curve at 2 K and it disappeared at 40 K.

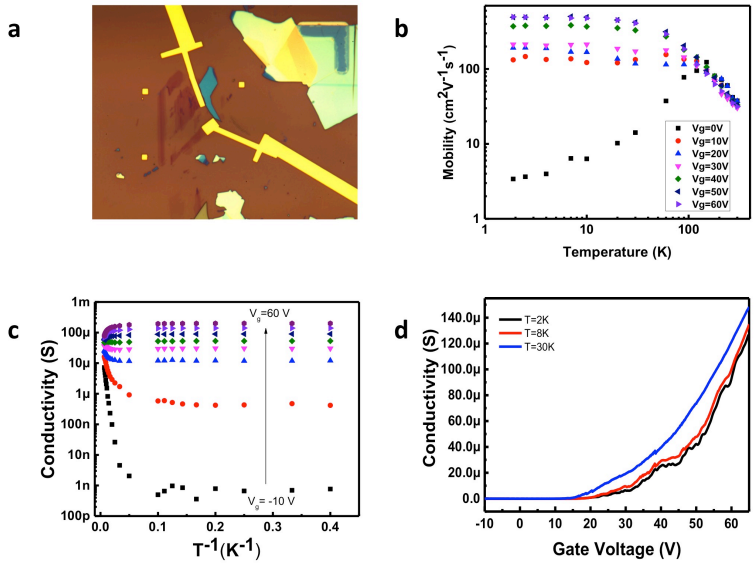

Figure 4.6 The optical microscope image and temperature-dependent electrical measurement of MoS_2 device. (a), The few-layer MoS_2 contacted by graphene electrodes. (b), Temperature-mobility relationship of few-layer device. With low gate voltage applied, the mobility decreases with lower temperature under 100 K, indicating the dominant impurity scattering at low gate voltage. Furthermore, the transition from dominant impurity scattering regime to a screened scattering regime happened at a lower gate voltage then the monolayer sample. (c), Temperature-conductivity relationship indicates two dominant transport mechanisms at high temperature and low temperature respectively. (d), Regularly distributed plateau in the transfer curves of few layer MoS_2 device with 0.5 mV source voltage

applied, indicating the presence of discrete localized states. The length of plateau is shorter than that of single layer sample.

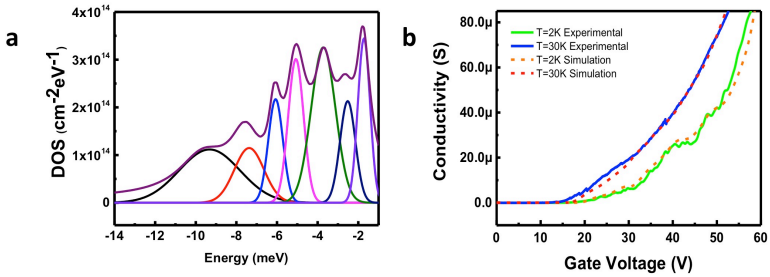

Figure 4.7 The simulated density of states and simulated transfer curves of few-layer MoS_2. (a), The density of localized states extracted from the conductivity plateau with variable range hopping model. 0mV is the mobility edge and the discrete localized states are enveloped in an exponentially decay function below the mobility edge. The density of localized states is lower than that of single layer device, leading to a more band-like transport. (b), The simulated transfer curves at 2 K and 30 K with the simulated localized states and the comparison to the corresponding experimental transfer curves.

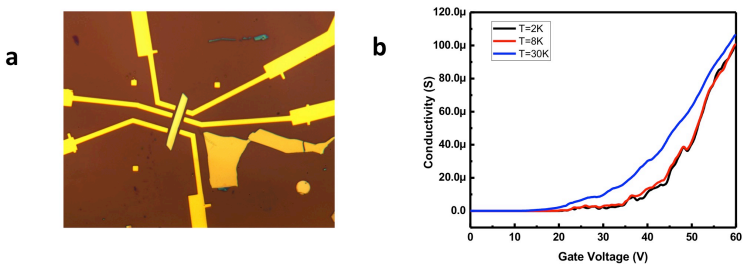

Figure 4.8 The optical microscope image of thick MoS_2 sample and its conductivity plateaus. (a), The optical microscope image of a thick MoS_2 device. (b), The transfer curves with excitation of 0.5 mV source voltage. The conductivity plateau is almost

negligible, indicating the density of localized states is even smaller compared to few-layer and monolayer sample.

References

1 Radisavljevic, B. & Kis, A. Mobility engineering and a metal-insulator transition in monolayer MoS_2. *Nat. Mater.* **12**, 815-820 (2013).

2 Ye, J. T. *et al.* Superconducting dome in a gate-tuned band insulator. *Science* **338**, 1193-1196 (2012).

3 Cui, X. *et al.* Multi-terminal transport measurements of MoS_2 using a van der Waals heterostructure device platform. *Nat. Nanotechnol.* **10**, 534-540 (2015).

4 Mak, K. F., Lee, C., Hone, J., Shan, J. & Heinz, T. F. Atomically thin MoS_2: A new direct-gap semiconductor. *Phys. Rev. Lett.* **105**, 136805 (2010).

5 Splendiani, A. *et al.* Emerging photoluminescence in monolayer MoS_2. *Nano Lett.* **10**, 1271-1275 (2010).

6 Kam, K. K. & Parkinson, B. A. Detailed photocurrent spectroscopy of the semiconducting group-VI transition-metal dichalcogenides. *J. Phys. Chem.* **86**, 463-467 (1982).

7 Sarkar, D. *et al.* A subthermionic tunnel field-effect transistor with an atomically thin channel. *Nature* **526**, 91-95 (2015).

8 Yap, W. C. *et al.* Layered material GeSe and vertical GeSe/MoS_2 p-n heterojunctions. *Nano Res.* doi: 10.1007/s12274-017-1646-8 (2017).

9 Cheng, R. *et al.* Few-layer molybdenum disulfide transistors and circuits for high-speed flexible electronics. *Nat. Commun.* **5**, 5143 (2014).

10 Mak, K. F., McGill, K. L., Park, J. & McEuen, P. L. The valley Hall effect in MoS_2 transistors. *Science* **344**, 1489-1492 (2014).

11 Amani, M. *et al.* Near-unity photoluminescence quantum yield in MoS_2. *Science* **350**, 1065-1068 (2015).

12 Tian, H. *et al.* Optoelectronic devices based on two-dimensional transition metal dichalcogenides. *Nano Res.* **9**, 1543-1560 (2016).

13 Yu, W. J. *et al.* Unusually efficient photocurrent extraction in monolayer van der Waals heterostructure by tunneling through discretized barriers. *Nat. Commun.* **7**, 13278 (2016).

14 Wan, X. *et al.* Controlled electrochemical deposition of large-area MoS_2 on graphene for high-responsivity photodetectors. *Adv. Funct. Mater.* **27**, 1603998 (2017).

15 Yu, Z. H. *et al.* Towards intrinsic charge transport in monolayer molybdenum disulfide by defect and interface engineering. *Nat. Commun.* **5**, 5290 (2014).

16 Liu, Y. *et al.* Toward barrier free contact to molybdenum disulfide using graphene electrodes. *Nano Lett.* **15**, 3030-3034 (2015).

17 Kaasbjerg, K., Thygesen, K. S. & Jacobsen, K. W. Phonon-limited mobility in n-type single-layer MoS_2 from first principles. *Phys. Rev. B* **85**, 115317 (2012).

18 Li, S. L. *et al.* Thickness-dependent interfacial coulomb scattering in atomically thin field-effect transistors. *Nano Lett.* **13**, 3546-3552 (2013).

19 Qiu, H. *et al.* Hopping transport through defect-induced localized states in molybdenum disulphide. *Nat. Commun.* **4**, 2642 (2013).

20 Yu, Z. *et al.* Analyzing the carrier mobility in transition-metal dichalcogenide MoS_2 field-effect transistors. *Adv. Funct. Mater.* **27**, 1604093 (2017).

21 Ghatak, S., Pal, A. N. & Ghosh, A. Nature of electronic states in atomically thin MoS_2 field-effect transistors. *ACS Nano* **5**, 7707-7712 (2011).

22 Hippalgaonkar, K. *et al.* High thermoelectric power factor in two-dimensional crystals of MoS_2. *Phys. Rev. B* **95**, 115407 (2017).

23 Tran, S. *et al.* Surface transport and quantum Hall effect in ambipolar black phosphorus double quantum wells. *Sci. Adv.* **3**, e1603179 (2017).

24 Hong, J. H. *et al.* Exploring atomic defects in molybdenum disulphide monolayers. *Nat. Commun.* **6**, 6293 (2015).

25 Lu, C. P., Li, G. H., Mao, J. H., Wang, L. M. & Andrei, E. Y. Bandgap, Mid-gap states, and gating effects in MoS_2. *Nano Lett.* **14**, 4628-4633 (2014).

26 Zhu, W. J. *et al.* Electronic transport and device prospects of monolayer molybdenum disulphide grown by chemical vapour deposition. *Nat Commun.* **5**, 3087 (2014).

27 Chen, X. L. *et al.* Probing the electron states and metal-insulator transition mechanisms in molybdenum disulphide vertical heterostructures. *Nat. Commun.* **6**, 6088 (2015).

28 Abrahams, E., Kravchenko, S. V. & Sarachik, M. P. Colloquium: Metallic behavior and related phenomena in two dimensions. *Rev. Mod. Phys.* **73**, 251-266 (2001).

29 Pallecchi, I. *et al.* Giant oscillating thermopower at oxide interfaces. *Nat. Commun.* **6**, 6678 (2015).

30 Das, S., Chen, H. Y., Penumatcha, A. V. & Appenzeller, J. High performance

multilayer MoS_2 transistors with scandium contacts. *Nano Lett.* **13**, 100-105 (2013).

31 Zhang, Y. B., Tan, Y. W., Stormer, H. L. & Kim, P. Experimental observation of the quantum Hall effect and Berry's phase in graphene. *Nature* **438**, 201-204, (2005).

32 Punnoose, A. & Finket'stein, A. M. Metal-insulator transition in disordered two-dimensional electron systems. *Science* **310**, 1429-1429 (2005).

33 Baugher, B. W. H., Churchill, H. O. H., Yang, Y. F. & Jarillo-Herrero, P. Intrinsic electronic transport properties of high-quality monolayer and bilayer MoS_2. *Nano Lett.* **13**, 4212-4216 (2013).

34 Chen, J. H., Jang, C., Xiao, S. D., Ishigami, M. & Fuhrer, M. S. Intrinsic and extrinsic performance limits of graphene devices on SiO_2. *Nat. Nanotechnol.* **3**, 206-209 (2008).

35 Steinberg, H., Gardner, D. R., Lee, Y. S. & Jarillo-Herrero, P. Surface state transport and ambipolar electric field effect in Bi_2Se_3 nanodevices. *Nano Lett.* **10**, 5032-5036 (2010).

36 Schmidt, H. *et al.* Transport properties of monolayer MoS_2 grown by chemical vapor deposition. *Nano Lett.* **14**, 1909-1913 (2014).

37 Das Sarma, S., Adam, S., Hwang, E. H. & Rossi, E. Electronic transport in two-dimensional graphene. *Rev. Mod. Phys.* **83**, 407-470 (2011).

38 Yoon, Y., Ganapathi, K. & Salahuddin, S. How good can monolayer MoS_2 transistors Be? *Nano Lett.* **11**, 3768-3773 (2011).

39 Kim, S. *et al.* High-mobility and low-power thin-film transistors based on multilayer MoS_2 crystals. *Nat. Commun.* **3,** 1011 (2012).

40 Gelmont, B., Shur, M. & Stroscio, M. Polar optical phonon scattering in three and two-dimensional electron gases. *J. Appl. Phys.* **77**, 657-660 (1995).

41 Jariwala, D. *et al.* Band-like transport in high mobility unencapsulated single-layer MoS_2 transistors. *Appl. Phys. Lett.* **102,** 173107 (2013).

42 Wu, J. *et al.* Large thermoelectricity via variable range hopping in chemical vapor deposition grown single-layer MoS_2. *Nano Lett.* **14**, 2730-2734 (2014).

43 Fowler, A. B., Timp, G. L., Wainer, J. J. & Webb, R. A. Observation of resonant tunneling in silicon inversion-layers. *Phys. Rev. Lett.* **57**, 138-141 (1986).

44 Guimaraes, M. H. D., Zomer, P. J., Vera-Marun, I. J. & van Wees, B. J. Spin-dependent quantum interference in nonlocal graphene spin valves. *Nano Lett.* **14**, 2952-2956 (2014).

45 Stone, A. D. & Lee, P. A. Effect of inelastic processes on resonant tunneling in one dimension. *Phys. Rev. Lett.* **54**, 1196-1199 (1985).

46 Liang, W. J. *et al.* Fabry-Perot interference in a nanotube electron waveguide. *Nature* **411**, 665-669 (2001).

47 Mucciolo, E. R., Neto, A. H. C. & Lewenkopf, C. H. Conductance quantization and transport gaps in disordered graphene nanoribbons. *Phys. Rev. B* **79**, 075407 (2009).

48 Nagy, A., Hundhausen, M., Ley, L., Brunst, G. & Holzenkampfer, E. Steady state hopping conduction in the conduction-band tail of a-Si-H studied in thin-film transistors. *Phys. Rev. B* **52**, 11289-11295 (1995).

49 Lin, Y. M., Perebeinos, V., Chen, Z. H. & Avouris, P. Electrical observation of

subband formation in graphene nanoribbons. *Phys. Rev. B.* **78,** 161409 (2008).

50 Seibel, C. *et al.* Quantized electronic fine structure with large anisotropy in ferromagnetic Fe films. *Phys. Rev. B* **90**, 035136 (2014).

Chapter 5 Derivations of hopping transport equation of MoS_2 field effect transistor

Introduction

In this chapter, I would derive the transport equation of the localized states in the MoS_2. As mentioned in the Chapter 4, the localized states transport in the cryogenic temperature regime is dominated by hopping and the transport will gradually transition into the ordinary band-like transport with increasing temperatures[1]. Therefore, a model including two types of states, which are the localized states and the extended states, would fit the case[2]. When the Fermi level is below the mobility edge ($E_F < E_C$), all the electrons in the material exist in localized states whose positions distributes in a quite wide range randomly. For the reason that the concentration of localization centers is relatively low, the distance between adjacent localization centers tends to be large, making the electron cannot transport freely from one hopping center to the adjacent ones. Therefore, the electrons have to be assisted by the energy of phonon and "hop" to other hopping centers[3]. As the phonon energy is proportional to the system temperature, for a system only consisting of localized states, its conductivity at zero Kelvin $\sigma = 0$, meaning that it is insulator. Only when temperature is not zero, electrons can absorb energy from phonons by thermal activation and then tunnel from one localization center to another generating hopping conductivity. In other words, hopping is a progress in which electrons tunnel from one localized state to another with the help of phonons. Such hopping process is called

variable range hopping as the hopping range varies and it was firstly studied by Mott[1]. It is discovered that the energy difference between the initial state and final state becomes smaller as the hopping distance becomes larger. Apart from the variable range hopping process, there is another hopping process called nearest neighbor hopping where the electron only hops between the nearest localization centers[4]. Usually the nearest hopping occurs in the system whose phonon energy is large enough and variable range hopping is a more generalized case.

Now consider the tunneling between two localized states that are located at $\boldsymbol{R_i}$ and $\boldsymbol{R_j}$ with energy E_i and E_j $(E_i > E_j)$. In quantum mechanics, the probability of which electrons tunnel from $\boldsymbol{R_i}$ to $\boldsymbol{R_j}$ through a distance $\left|\boldsymbol{R_i} - \boldsymbol{R_j}\right|$ is in proportion to the square of the overlap integral of the wave functions localized at i and j. For localized states, the wave function can be simplified using $\psi(\boldsymbol{r} - \boldsymbol{R_i}) \propto \exp(-|\boldsymbol{r} - \boldsymbol{R_i}|/\lambda)$ where λ is localization length[5]. For simplicity, the localization lengths of localized states are approximated as the same value. So, the overlap integral can be expressed in the form

$$\int \psi^*(\boldsymbol{r} - \boldsymbol{R_i})\psi(\boldsymbol{r} - \boldsymbol{R_j})\mathrm{d}^3 r \propto \exp\left(-\frac{R}{\lambda}\right) \quad (1)$$

Thus, the tunneling probability between $\boldsymbol{R_i}$ and $\boldsymbol{R_j}$ localized states are in proportion to $\exp(-2\alpha R)$, where $\alpha^{-1} \equiv \lambda$. On the other hand, difference exists between the energies of initial hopping state and the final hopping state. The energy difference $W = E_j - E_i$ (> 0) is needed by the hopping process from site at $\boldsymbol{R_i}$ to site at $\boldsymbol{R_j}$ and the energy must be provided by phonons. As a result, although there is significant

overlap between two adjacent localized state wave functions, electrons cannot overcome the energy difference W between two localized state wave functions without phonons at $T = 0\mathrm{K}$ and the transition probability is zero. When the temperature is non-zero, the distribution of thermal phonons with energy W is $[\exp(W/k_BT) - 1]^{-1}$, which can be simplified with Boltzmann factor $\exp(-W/k_BT)$ when $k_BT \ll W$. Therefore, the hopping probability from state at $\boldsymbol{R_i}$ to the state at $\boldsymbol{R_j}$ is not only in proportion to the hopping probability $\exp(-2\alpha R)$ but also the number of the phonons in thermal equilibrium. Adding the phonon term $\exp(-W/k_BT)$, the hopping probability can be written as:

$$w_{ij} = w_0 \exp\left(-2\alpha R - \frac{W}{k_BT}\right), W = E_j - E_i > 0 \quad (2)$$

This is the basic equation for both nearest-neighbor hopping and variable range hopping, where w_{ij} represents the probability hopping from occupied state i to empty state j per second.

Nearest neighbor hopping conductivity

Nearest neighbor hopping occurs between the adjacent localization centers where $R = R_0$ is the average distance. Supposing that the concentration of the impurities in the disordered system is n_I and according to the condition $(4\pi/3)R_0^3 n_\mathrm{I} = 1$, we have

$$R_0 = \left(\frac{3}{4\pi n_\mathrm{I}}\right)^{\frac{1}{3}} \quad (3)$$

Besides, for nearest neighbor hopping process, the term $\exp(-2\alpha R_0)$ is a constant.

Especially in weak localization situation $\alpha R_0 \leq 1$ and $\exp(-2\alpha R_0)$ can even be ignored. On the other hand, the energy term in the equation (1) plays a more significant role. Assume the energy W_0 is the average energy needed by electrons transiting between adjacent localization centers. Thus, the nearest neighbor hopping occurs often at the temperature when there are enough phonons with energy W_0 provided. The conductivity can be written in the form of thermal activation:

$$\sigma(T) = \sigma_0 \exp\left(-\frac{W_0}{k_B T}\right) \tag{4}$$

Variable range hopping conductivity

When the temperature is further decreased and the number and energy of the thermal activated phonon are small, there is nearly no phonons with energy W_0 assisting nearest neighbor hopping. But electrons can still absorb lower energy phonons ($W < W_0$) and hop to the localized states whose distances are further but energy differences are smaller. When R is large, the relation between W and R can be obtained from density of states, $N(E)$. In a state variable sphere with its center at localized state $\boldsymbol{R_i}$ and radius R, the number of states with energy between E and $E + \Delta E$ is $(4\pi/3)R^3 N(E)\Delta E$. Considering that the dominant contribution of conductivity comes from electron transition between localized states near Fermi level E_F, it is rational to assume that the initial localized state E_i and final E_j are both in a small range of W near E_F and moreover $E_j = E_i + W$ as the energy is conservative. As there is one available hopping state in this sphere,

$$\frac{4\pi}{3}R^3N(E_F)W = 1 \tag{5}$$

where $W = E_j - E_i,\ E_j > E_i$.

Thus,

$$W(R) = \frac{3}{4\pi R^3 N(E_F)} \tag{6}$$

This equation holds only when W is small and R is large. The transition probability between state at $\boldsymbol{R_i}$ and the state at $\boldsymbol{R_j}$ is in proportion to $\exp\{-2\alpha R - [W(R)/k_BT]\}$, where we can see that the two factors in the exponential term have opposite tendencies against varying R. In other words, although the overlap factor of wave functions $\exp(-2\alpha R)$ decreases as R increasing, the compensation can be gotten from $\exp[-W(R)/k_BT]$, the Boltzmann factor of phonons absorbed, due to the fact that W decreases rapidly as R increases. As a result, for a some R, the hopping probability reaches its maximum.

$$Q(R) \equiv 2\alpha R + W(R)/k_BT \tag{7}$$

The maximum of $Q(R)$ can be obtained when

$$\frac{\mathrm{d}Q(R)}{\mathrm{d}R} = \frac{\mathrm{d}}{\mathrm{d}R}\left[2\alpha R + \frac{3}{4\pi R^3 N(E_F)k_BT}\right] = 0 \tag{8}$$

Thus, the most probable hopping distance is

$$\bar{R} = \left[\frac{9}{8\pi\alpha N(E_F)k_BT}\right]^{\frac{1}{4}} \tag{9}$$

Obviously, $\bar{R}$ increases as temperature decreases. Substituting $\bar{R}$ in to Q, we can get the most transition probability is in proportion to

$$\exp[-Q(R)] = \exp\left[-\frac{8}{3}\alpha\bar{R}\right] = \exp\left\{-\frac{8}{3}\alpha\left[\frac{9}{8\pi\alpha N(E_F)k_BT}\right]^{\frac{1}{4}}\right\} = \exp\left(-B/T^{\frac{1}{4}}\right) \tag{10}$$

where

$$B \equiv \frac{8}{3}\left(\frac{9}{4\pi}\right)^{\frac{1}{4}}\left[\frac{\alpha^3}{k_B N(E_F)}\right]^{\frac{1}{4}} \approx 2\left[\frac{\alpha^3}{k_B N(E_F)}\right]^{\frac{1}{4}} \quad (11)$$

Substituting equation (9) into equation (3), we can obtain the variable range hopping conductivity:

$$\sigma(T) = \sigma_0 \exp[-Q(\bar{R})] = \sigma_0 \exp\left(-B/T^{\frac{1}{4}}\right) \quad (12)$$

The above formula is the famous Mott's $T^{\frac{1}{4}}$ law, which is the characteristics of the VRH conductivity in 3-D disordered systems[6]. For d dimensions ($d = 1,2,3$) systems, we can derive the conductivity in a similar way and obtain

$$\sigma(T) = \sigma_0 \exp\left(-B/T^{\frac{1}{d+1}}\right) \quad (13)$$

When fitting the $\ln\sigma$ in a linear relationship against $T^{-1/4}$, the slope is $-B$. The fitting results are illustrated in the Table 5.1. According to the fitting results, the localization length λ is approximately 25Å.

Calculations of density of states of localized states

Following the derived variable range hopping conductivity model, the density of state of localized states can also be obtained using the model.

Firstly, the conductivity can be represented in the form of an integral of the differential conductivity:

$$\sigma(T) = \int \sigma(E,T)\mathrm{d}E = \int e g_{\mathrm{bt}}(E) f(E,T)\mu(E,T)\mathrm{d}E \quad (14)$$

where g_{bt} is the density of states near the conduction band tail. $f(E,T) = 1/\{1+\exp[(E-E_F)/k_BT]\}$ is the Fermi-Dirac distribution function. The differential hopping mobility $\mu(E,T)$ is dependent with the energy of electrons and

the temperature. According to the Einstein's relation, we can obtain the differential mobility μ via calculating the diffusion coefficient $D(E,T)$:

$$\mu(E,T) = D(E,T)\frac{e}{k_B T} \tag{15}$$

Consider the material whose electrons do not distribute uniformly only in one direction. We can divide the material into several parallel planes normal to this direction and set the distance between planes to be hopping distance R.

Assuming that there is an electron in a localized state in plane 1 and it is in thermal motion at a frequency ν. The thermal motion means will cause the electron attempt to move in all the directions, therefore the frequency of the motion which leads to plane 2 is $\frac{1}{6}\nu$ in the three-dimensional case (in two-dimensional case it's $\frac{1}{4}\nu$). As illustrated in Figure 5.1, if the densities of electrons in plane 1 and plane 2 are n_1 and n_2, the net flux from plane 1 to plane 2 is

$$j = \frac{1}{6}(n_1 - n_2)\nu = \frac{1}{6}(c_1 R - c_2 R)\nu = \frac{1}{6}R^2\frac{\mathrm{d}c}{\mathrm{d}x}\nu \tag{16}$$

Thus

$$D = \frac{1}{6}R^2\nu \tag{17}$$

Also, according to the previous analysis, $\nu = \nu_0 \exp(-2\alpha R)\exp(-W/k_B T)$. Therefore, the diffusion constant can be obtained:

$$D_{ij} = \frac{1}{6}R_{ij}^2\nu_{ij} = \frac{1}{6}R_{ij}^2\nu_0 \exp\left(-\frac{2R_{ij}}{\lambda}\right) \times \begin{cases} \exp\left(\frac{E_i - E_j}{k_B T}\right), \text{for } E_j \geq E_i \\ 1, \text{for } E_j < E_i \end{cases} \tag{18}$$

where E_i and E_j represent the energy of the initial state and final state. λ is the localization length which has the relation with energy $\lambda(E) \propto (E_C - E)^{-0.5}$ [7].

In the fitting of MoS_2 localized state transport, the localization length has the form $\lambda = 25[(E_C - E)/0.8\text{eV}]^{-0.5}$Å. ν_0 is the attempt frequency and its range is usually $10^{12}\text{s}^{-1} < \nu_0 < 10^{13}\text{s}^{-1}$. Here $\nu_0 \simeq 4\times10^{11}\text{s}^{-1}$ is utilized for the MoS_2 transport at low temperature.

Dealing the hopping of each individual localized states to get the exact D_{ij} is a computationally impossible task for us. Therefore, the average $\overline{D}(E)$ is evaluated instead by calculating the average hopping distance $\bar{R}(E)$[8]. It is easy to know that the relation between the average distance and the average concentration of the vacant states:

$$\bar{R}(E) = N_{\text{f}}^{-1/3} \tag{19}$$

Furthermore, N_{f} can be divided into two parts: one consists of the states with energy below E $(N_1(E))$ and the other consists of those with energy higher than E $(N_2(E))$:

$$N_{\text{f}}(E) = N_1(E) + N_2(E) \tag{20}$$

Where by definition

$$N_1(E) = \int_{-\infty}^{E} g_{\text{bt}}(\varepsilon)[1 - f(\varepsilon)]\text{d}\varepsilon \tag{21}$$

and

$$N_2(E) = \int_{E}^{\infty} g_{\text{bt}}(\varepsilon)[1 - f(\varepsilon)] \exp\left(\frac{E-\varepsilon}{k_B T}\right) \text{d}\varepsilon \tag{22}$$

where the hopping probability $\exp[(E - \varepsilon)/k_B T]$ is considered to obtain the average value.

By calculating the results of the above formulas, the average value of hopping distance $\bar{R}(E)$ can be obtained.

Therefore, the average diffusion coefficient $\overline{D}(E)$ will be

$$\overline{D}(E) = \frac{1}{6}\bar{R}^2(E)\nu_0 \exp\left[\frac{-2\bar{R}(E)}{\lambda}\right] \tag{23}$$

As a result, the hopping conductivity

$$\sigma(E_F, T) = \frac{e^2\nu_0}{k_B T}\int g_{\mathrm{bt}}(\varepsilon) f_{E_F}(\varepsilon, T)\frac{1}{6}\bar{R}^2(\varepsilon)\exp\left[\frac{-2\bar{R}(\varepsilon)}{\lambda}\right]\mathrm{d}\varepsilon \tag{24}$$

Theoretically, knowing the relation $\sigma(E_F)\sim E_F$, we can solve this non-linear integral equation to get g_{bt} with Newton iterative method. However, experimentally we can only obtain the relation of $\sigma\sim \mathrm{V_G}$. In order to obtain $\sigma(\mathrm{E_F})\sim \mathrm{E_F}$, the relationship between gate oxide voltage and induced charge was utilized:

$$Q = C_{\mathrm{ox}}V_G \approx \int_{E_{Fo}}^{E_F} g_{\mathrm{bt}}(\varepsilon)\mathrm{d}\varepsilon \tag{25}$$

So far, the method to obtain the density of state of the MoS_2 localized state has been derived. The solution can be obtained numerically but the computation cost is still beyond our capability. Therefore, in order to speed up the calculation, the equation is vectorized and the parallel computation architecture can be leveraged.

To discretize the equation, we start from the concentration of the hopping electron near the Fermi level, $N_{\mathrm{f}}(E)$:

$$N_{\mathrm{f}}(E) = N_1(E) + N_2(E) = \int_{-\infty}^{E} g_{\mathrm{bt}}(\varepsilon)[1 - f(\varepsilon)]\mathrm{d}\varepsilon + \int_{E}^{\infty} g_{\mathrm{bt}}(\varepsilon)[1 -$$

$$f(\varepsilon)]\exp\left(\frac{E-\varepsilon}{k_BT}\right)\mathrm{d}\varepsilon = \int_{-\infty}^{\infty} g_{\mathrm{bt}}(\varepsilon)[1-f(\varepsilon)]\begin{cases}\exp\left(\frac{E-\varepsilon}{k_BT}\right), \varepsilon \geq E \\ 1, \varepsilon < E\end{cases}\mathrm{d}\varepsilon = \int g_{\mathrm{bt}}(\varepsilon)[1-$$

$$f(\varepsilon)]p_{\mathrm{B}}(E,\varepsilon)\mathrm{d}\varepsilon \qquad (26)$$

where the piecewise function $p_{\mathrm{B}}(E,\varepsilon)$ can be expressed with matrix:

$p_{\mathrm{B}}(E,\varepsilon) =$

$$\begin{bmatrix} 1 & \cdots & \exp\left(\frac{E_1-\varepsilon_i}{k_BT}\right) & \cdots & \cdots & \cdots & \exp\left(\frac{E_1-\varepsilon_{\mathrm{end}}}{k_BT}\right) \\ \vdots & & \ddots & \ddots & & & \vdots \\ 1 & \cdots & \cdots & \exp\left(\frac{E_m-\varepsilon_j}{k_BT}\right) & \cdots & \cdots & \exp\left(\frac{E_m-\varepsilon_{\mathrm{end}}}{k_BT}\right) \\ \vdots & & & \ddots & \ddots & & \vdots \\ 1 & \cdots & \cdots & \cdots & \exp\left(\frac{E_{\mathrm{end}}-\varepsilon_k}{k_BT}\right) & \cdots & \exp\left(\frac{E_{\mathrm{end}}-\varepsilon_{\mathrm{end}}}{k_BT}\right) \end{bmatrix} = [p_{ij}] \qquad (27)$$

Therefore, the vacant state concentration can be calculated approximately in the discretized form:

$$N_{\mathrm{f}}(E_i) = N_{\mathrm{fi}} = \Delta\varepsilon \sum_j g_{\mathrm{bt}j}\left(1-f_{E_Fj}\right)p_{ij} \qquad (28)$$

and the energy-dependent localization length can also be written as[7,9]

$$\lambda(E_i) = \lambda_i = 25\left(\frac{E_C-E_i}{0.8\mathrm{eV}}\right)^{-0.5}\text{ Å} \qquad (29)$$

Finally, the conductivity is obtained approximately with the formula below:

$$\sigma(E_F,T) = e\Delta E\sum_i g_{\mathrm{bt}i}f_{E_Fi}\mu_i = \frac{e^2\Delta E}{k_BT}\sum_i g_{\mathrm{bt}i}f_{E_Fi}D_i =$$

$$\frac{e^2\nu_0\Delta E}{6k_BT}\sum_i g_{\mathrm{bt}i}f_{E_Fi}\left(\Delta\varepsilon\sum_j g_{\mathrm{bt}j}\left(1-\right.\right.$$

$$\left.\left.f_{E_Fj}\right)p_{ij}\right)^{-2/3}\exp\left(-\frac{2\left(\Delta\varepsilon\sum_j g_{\mathrm{bt}j}\left(1-f_{E_Fj}\right)p_{ij}\right)^{-1/3}}{25\left(\frac{E_C-E_i}{0.8\mathrm{eV}}\right)^{-0.5}}\right) \qquad (30)$$

Furthermore, we can change the relation of $\sigma\sim E_F$ into $\sigma\sim V_G$ to make it more convenient fitting the experimental data. Assuming that the gate voltage data array $V_{G1}, V_{G2}, \cdots, V_{G\mathrm{end}}$ has same increment, we are able discretize the energy increment,

$\mathrm{d}E$, respectively. Specifically, the gate voltage array can be also represented as,

$$\frac{\mathrm{d}VC_{\mathrm{ox}}}{eg_{\mathrm{bt1}}}, \frac{\mathrm{d}VC_{\mathrm{ox}}}{eg_{\mathrm{bt1}}} + \frac{\mathrm{d}VC_{\mathrm{ox}}}{eg_{\mathrm{bt2}}}, \cdots, \frac{\mathrm{d}VC_{\mathrm{ox}}}{eg_{\mathrm{bt1}}} + \cdots + \frac{\mathrm{d}VC_{\mathrm{ox}}}{eg_{\mathrm{btend}}} \tag{31}$$

Therefore, the increments of energy $\mathrm{d}E$ can also be presented as an array.

$$\frac{\mathrm{d}VC_{\mathrm{ox}}}{eg_{\mathrm{bt1}}}, \frac{\mathrm{d}VC_{\mathrm{ox}}}{eg_{\mathrm{bt2}}}, \cdots, \frac{\mathrm{d}VC_{\mathrm{ox}}}{eg_{\mathrm{btend}}} \tag{32}$$

Then substitute (32) into (26), we have

$$N_{\mathrm{f}}(E_i) = \frac{\mathrm{d}VC_{\mathrm{ox}}}{eg_{\mathrm{bt1}}} g_{\mathrm{bt1}} \left(1 - \frac{1}{1+\exp\left[-\frac{\mathrm{d}VC_{\mathrm{ox}}}{ek_BT}\left(\frac{1}{g_{\mathrm{bt2}}}+\cdots+\frac{1}{g_{\mathrm{bt}m}}\right)\right]}\right) + \cdots + \frac{\mathrm{d}VC_{\mathrm{ox}}}{eg_{\mathrm{bt}i+1}} g_{\mathrm{bt}i+1} \left(1 - \frac{1}{1+\exp\left[\frac{\mathrm{d}VC_{\mathrm{ox}}}{ek_BT}\left(\frac{1}{g_{\mathrm{bt}m+1}}+\cdots+\frac{1}{g_{\mathrm{bt}i+1}}\right)\right]}\right) \exp\left[-\frac{\mathrm{d}VC_{\mathrm{ox}}}{ek_BT}\left(\frac{1}{g_{\mathrm{bt}i+1}}\right)\right] + \cdots + \frac{\mathrm{d}VC_{\mathrm{ox}}}{eg_{\mathrm{btend}}} g_{\mathrm{btend}} \left(1 - \frac{1}{1+\exp\left[\frac{\mathrm{d}VC_{\mathrm{ox}}}{ek_BT}\left(\frac{1}{g_{\mathrm{bt}m+1}}+\cdots+\frac{1}{g_{\mathrm{btend}}}\right)\right]}\right) \exp\left[-\frac{\mathrm{d}VC_{\mathrm{ox}}}{ek_BT}\left(\frac{1}{g_{\mathrm{bt}i+1}}+\cdots+\frac{1}{g_{\mathrm{btend}}}\right)\right] =$$

$$\frac{\mathrm{d}VC_{\mathrm{ox}}}{e} \exp\left[\frac{\mathrm{d}VC_{\mathrm{ox}}}{ek_BT}\left(\frac{1}{g_{\mathrm{bt}m+1}}+\cdots+\frac{1}{g_{\mathrm{bt}i}}\right)\right] \left\{\frac{\exp\left[-\frac{\mathrm{d}VC_{\mathrm{ox}}}{ek_BT}\left(\frac{1}{g_{\mathrm{bt2}}}+\cdots+\frac{1}{g_{\mathrm{bt}i}}\right)\right]}{1+\exp\left[-\frac{\mathrm{d}VC_{\mathrm{ox}}}{ek_BT}\left(\frac{1}{g_{\mathrm{bt2}}}+\cdots+\frac{1}{g_{\mathrm{bt}m}}\right)\right]} + \cdots + \frac{1}{1+\exp\left[\frac{\mathrm{d}VC_{\mathrm{ox}}}{ek_BT}\left(\frac{1}{g_{\mathrm{bt}m+1}}+\cdots+\frac{1}{g_{\mathrm{bt}i+1}}\right)\right]}\right\}$$

$$+ \cdots + \frac{1}{1+\exp\left[\frac{\mathrm{d}VC_{\mathrm{ox}}}{ek_BT}\left(\frac{1}{g_{\mathrm{bt}m+1}}+\cdots+\frac{1}{g_{\mathrm{btend}}}\right)\right]}\Bigg\} \tag{33}$$

Then $\bar{R}(E_i)$ and the conductivity can also be expressed and obtained in a similar way. After modifying the calculation in this way, the relationship of DOS vs. gate voltage can be calculated. Finally, the $\sigma \sim V_G$ results are also calculated for the comparison with the experimental data.

In the calculation progress, in addition to determining the position of the Fermi level, we also have to assume that the DOS has a contribution according to the most probable range of the localized states. To estimate the range, the relation of $\sigma \sim 1/T$ in the band-like transport regime is utilized. In the thermal activated hopping range,

the carrier is activated from the localized states to the conduction band and then transport freely in the extended state. So, the activation energy is a good measure to estimate the position of the localized states in the band gap as mentioned in the Chapter 4. Using the temperature conductivity of MoS_2 above 30 K, the range of localized states is estimated to be around 10 meV.

Finally, it is also necessary to consider the conduction contribution from the electrons activated to the extended states. The expansion of the Fermi distribution function's tail is about 10 meV which is comparable to the expansion of the conduction band tail and will sweep into the conduction band. Thus, the electrons in the conduction band are also involved in the conduction. For this reason, we have to combine the hopping conductivity with thermal activation. The conductivity at extended state is in proportion to the number of the electrons in the conduction band, which is in proportion to the Fermi distribution function $f = 1/\{1 + \exp[(E_C - E_F)/k_B T]\}$. For the low gate voltage which cannot fill the electrons into the conduction band, $\exp[(E_C - E_F)/k_B T] \gg 1$, making the conductivity approximately proportional to $\exp[-(E_C - E_F)/k_B T]$, which is in agreement with the thermal activated transport $\sigma \propto \exp(-1/T)$.

Calculations results and discussions

After combining the variable range hopping conductivity at low temperature with the

thermal activation at high temperature, by fitting the experimental data of $\sigma \sim V_G$ at low V_{DS}, the density of localized states in the conduction band tail can be obtained.

As illustrated in the Figure 5.2 (a), the conductivity at T=30 K is affected by the mobility of electrons in the conduction band. As the gate voltage increases, the Fermi level approaches closer to the extended states, making the band-like transport plays the more significant roles. Therefore, the change of mobility induces larger change of conductivity in the high gate voltage regime. Oppositely, as the temperature decreases, the contribution from the extended states becomes more trivial and the conductivity is nearly independent of the extended states mobility (Figure 5.2 (b)). Besides, in Figure 5.2 (a) and (b), it can be seen that when $V_G < 10\,\mathrm{V}$, the conductivity is nearly zero because the Fermi level is not in the range of localized states (band tail) yet. While $V_G > 20\,\mathrm{V}$ the conductivity significantly increased as the Fermi level enters the energy range of localized states.

We can obtain the simulation results which are in agreements with the experimental data at 2 K and 30 K when assuming the electrons in conduction band have a constant mobility $1000\mathrm{cm}^2/(\mathrm{V}\cdot\mathrm{s})$, which is in the agreement with the experiment[10]. The width of the localized states is about 7 meV. We would like to note that due to the reason that the Fermi level does not the energy level of the localized states until the gate voltage is about 20 V, it is necessary to assume that there are also some states existing in the energy gap and the DOS is $1.5\times10^{13}\mathrm{cm}^{-2}\mathrm{eV}^{-1}$. The fitting also

depends on the position of E_F at $V_G = 0$, which cannot be obtained from the experimental data. However, this will not affect the form of localized states.

Conclusions

In conclusion, the transport equation of electron transport in MoS_2 at low temperature is derived in the framework of variable range hopping and band like transport theories. In the equation, the conductivity becomes a function of localized states density and the mobility of extended state in the conduction band. By fitting the experimental transfer curves with different conduction band mobility, the localized state density can be obtained. Finally, it is found that the conductivity gradually transitions from the band-like transport to the variable range hopping as temperature decreases or gate voltage decreases.

Table and Figures

V_G (V)	10	20	30	40	50	60
B	-4.93	-2.99	-1.75	-1.05	-0.48	-0.14

Table 5.1 The linear fitting of experimental data according to Mott's $T^{\frac{1}{4}}$ law. The average carrier density is selected as $N = 5\times10^{23}\text{cm}^{-3}\text{eV}^{-1}$ in the calculations.

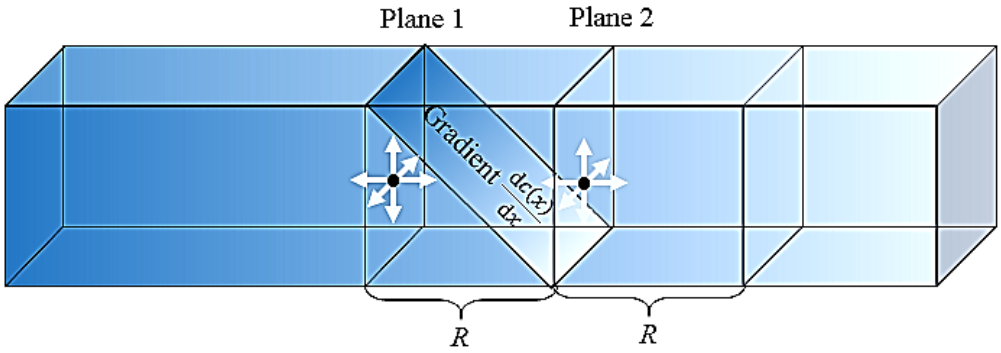

Figure 5.1 The schematic of electron diffusion in the material.

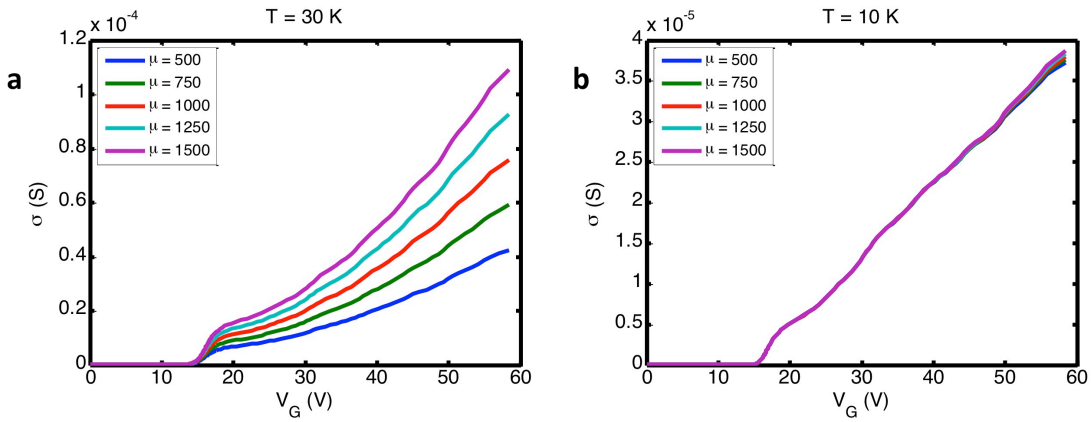

Figure 5.2 The simulated transfer curves with different extended state mobility (a), The simulated conductivity as a function of back gate voltage at T =30 K. The conductivity also increases as the extended state mobility increases. (b), The simulated conductivity as a function of back gate voltage at T = 10 K. The conductivity is almost independent of the extended states as the hopping transport is the dominant transport in the low temperature regime.

References

1 Mott, N. F. Conduction in Non-Crystalline Materials .III. Localized States in a Pseudogap and near Extremities of Conduction and Valence Bands. *Philos Mag* **19**, 835-852 (1969).

2 Zhu, W. J. *et al.* Electronic transport and device prospects of monolayer molybdenum disulphide grown by chemical vapour deposition. *Nat Commun* **5** 3087 (2014).

3 Yu, D., Wang, C. J., Wehrenberg, B. L. & Guyot-Sionnest, P. Variable range hopping conduction in semiconductor nanocrystal solids. *Phys Rev Lett* **92** 216802 (2004).

4 Kirkpatrick, S. Percolation and Conduction. *Rev Mod Phys* **45**, 574-588 (1973).

5 Yoshino, S. & Okazaki, M. Numerical Study of Electron Localization in Anderson Model for Disordered Systems - Spatial Extension of Wavefunction. *J Phys Soc Jpn* **43**, 415-423 (1977).

6 Mott, N. F. Conduction in Non-Crystalline Systems .I. Localized Electronic States in Disordered Systems. *Philos Mag* **17**, 1259-1268 (1968).

7 Abram, R. A. & Edwards, S. F. The nature of the electronic states of a disordered system. II. Extended states. *Journal of Physics C: Solid State Physics* **5**, 1196 (1972).

8 Fritzsche, H. Low-Temperature Electronic Transport in Non-Crystalline Semiconductors. *J Non-Cryst Solids* **114**, 1-6 (1989).

9 Nagy, A., Hundhausen, M., Ley, L., Brunst, G. & Holzenkampfer, E. Steady-State Hopping Conduction in the Conduction-Band Tail of a-Si-H Studied in Thin-Film

Transistors. *Phys Rev B* **52**, 11289-11295 (1995).

10 Liu, Y. *et al.* Toward Barrier Free Contact to Molybdenum Disulfide Using Graphene Electrodes. *Nano Lett* **15**, 3030-3034 (2015).